remote sensing

MDPI

Article

Improving Typhoon Muifa (2022) Forecasts with FY-3D and FY-3E MWHS-2 Satellite Data Assimilation under Clear Sky Conditions

Feifei Shen [1,2,3], Xiaolin Yuan [1], Hong Li [4], Dongmei Xu [1,2,*], Jingyao Luo [4], Aiqing Shu [1] and Lizhen Huang [1]

[1] Key Laboratory of Meteorological Disaster, Ministry of Education (KLME)/Joint International Research Laboratory of Climate and Environment Change (ILCEC)/Collaborative Innovation Center on Forecast and Evaluation of Meteorological Disasters (CIC-FEMD), Nanjing University of Information Science & Technology, Nanjing 210044, China; ffshen@nuist.edu.cn (F.S.); 202312050017@nuist.edu.cn (X.Y.); 20211201033@nuist.edu.cn (A.S.); 202212010158@nuist.edu.cn (L.H.)
[2] State Key Laboratory of Severe Weather, Chinese Academy of Meteorological Sciences, Beijing 100081, China
[3] China Meteorological Administration Tornado Key Laboratory, Guangzhou 510641, China
[4] Shanghai Typhoon Institute, China Meteorological Administration, Shanghai 200030, China; lih@typhoon.org.cn (H.L.); luojy@typhoon.org.cn (J.L.)
* Correspondence: dmxu@nuist.edu.cn

Abstract: This study investigates the impacts of assimilating the Microwave Humidity Sounder II (MWHS-2) radiance data carried on the FY-3D and FY-3E satellites on the analyses and forecasts of Typhoon Muifa in 2022 under clear-sky conditions. Data assimilation experiments are conducted using the Weather Research and Forecasting (WRF) model coupled with the Three-Dimensional Variational (3D-Var) Data Assimilation method to compare the different behaviors of FY-3D and FY-3E radiances. Additionally, the data assimilation strategies are assessed in terms of the sequence of applying the conventional and MWHS-2 radiance data. The results show that assimilating MWHS-2 data is able to enhance the dynamic and thermal structures of the typhoon system. The experiment with FY-3E MWHS-2 assimilated demonstrated superior performance in terms of simulating the typhoon's structure and providing a prediction of the typhoon's intensity and track than the experiment with FY-3D MWHS-2 did. The two-step assimilation strategy that assimilates conventional observations before the radiance data has improved the track and intensity forecasts at certain times, particularly with the FY-3E MWHS-2 radiance. It appears that large-scale atmospheric conditions are more refined by initially assimilating the Global Telecommunication System (GTS) data, with subsequent satellite data assimilation further adjusting the model state. This strategy has also confirmed improvements in precipitation prediction as it enhances the dynamic and thermal structures of the typhoon system.

Keywords: MWHS-2 radiance; data assimilation; clear sky; typhoon forecast

Citation: Shen, F.; Yuan, X.; Li, H.; Xu, D.; Luo, J.; Shu, A.; Huang, L. Improving Typhoon Muifa (2022) Forecasts with FY-3D and FY-3E MWHS-2 Satellite Data Assimilation under Clear Sky Conditions. *Remote Sens.* **2024**, *16*, 2614. https://doi.org/10.3390/rs16142614

Academic Editor: Mark Bourassa

Received: 23 May 2024
Revised: 12 July 2024
Accepted: 13 July 2024
Published: 17 July 2024

1. Introduction

Satellite observations enhance the accuracy of numerical weather prediction (NWP) by enabling comprehensive monitoring of the Earth's surface across vast geographical extents [1–6]. These observations provide extensive atmospheric parameters, such as temperature, humidity, cloud cover, and precipitation. Through the assimilation of satellite data, the initial state of the model can be adjusted to better match the actual atmospheric conditions, resulting in more reliable forecasts [7,8].

The utilization of satellite microwave data has significantly influenced NWP, particularly with the emphasis on microwave-sounding instruments [9–11]. Microwave radiation is able to penetrate the cloud, haze, and atmospheric water vapor, allowing satellite microwave data to be collected regardless of weather conditions [12,13]. Shen et al. [14] investigated the impact of assimilating radiances from the Advanced Microwave Sounding Unit-A (AMSU-A) on the track prediction of Typhoon Megi. Their findings underscored a

notable enhancement in track forecast accuracy with the utilization of hybrid data assimilation (DA). Choudhury et al. [15] employed the Hybrid-4DVar assimilation and forecast system of the National Centre for Medium Range Weather Forecast's (NCMRWF) Unified Model (NCUM) to assess the influence of sounder for probing vertical profiles of humidity (SAPHIR) radiance data assimilation on enhancing the accuracy of tropical cyclone track and intensity forecasts in three case studies. Their study discovered that the assimilation of SAPHIR radiances led to respective improvements in the central sea level pressure (CSLP) and in the maximum sustained wind (MSW) of the cyclones as well as in the cyclone tracks. An investigation conducted by Dhanya et al. [16] aimed at assessing the impact of assimilating SAPHIR radiances on tropical cyclone modeling within the Indian region. According to their study, the assimilation of SAPHIR data into the model leads to enhancements across various cyclone-related variables. These improvements encompass the depiction of minimum sea level pressure, maximum wind speed, track prediction accuracy, warm core structure, relative vorticity structure, and precipitation simulation. Similarly, the Advanced Technology Microwave Sounder (ATMS) data obtained from the Suomi National Polar-Orbiting Partnership (NPP) satellite was utilized by Xie et al. [17] to acquire temperature and humidity information for weather prediction models. The results revealed a significant enhancement in the accuracy and skill of rainfall prediction, especially in forecasting heavy rainfall events. The assimilation of ATMS radiance data improved both the spatial distribution and threat scores of precipitation forecasts, reducing false alarms. Lai et al. [18] applied the Three-Dimensional Variational Data Assimilation (3D-Var) method to assimilate the AMSU-A radiance data, which indicates a notable enhancement in tropical cyclone (TC) track forecast accuracy.

The deployment of FY-3A in May 2008 marked the initiation of China's Fengyun-3 series of satellites (FY-3) [19]. FY-3A and FY-3B are equipped with the Microwave Humidity Sounder I (MWHS-1) instruments, while FY-3C, FY-3D, and FY-3E [20,21] are equipped with the advanced MWHS-2 instruments. Reputable meteorological institutions such as the European Centre for Medium-Range Weather Forecasts (ECMWF) and the UK Met Office have emphasized the reliability and practicality of MWHS-2 data from both FY-3D and FY-3E satellites [22–24], thereby highlighting the increasing importance of MWHS-2 observations in assimilation systems [25]. Recent studies have demonstrated the effectiveness of the MWHS-2 instruments on the FY-3D and FY-3E satellites in enhancing weather prediction capabilities. Xu et al. [26] investigated the impact of assimilating FY-3D MWHS-2 radiance data under clear-sky conditions on the simulation of the tropical storm Ampil. Their study confirmed the effectiveness of bias correction for the humidity sounder, resulting in a well-matched analysis field following radiance data assimilation. A study was conducted by Xiao et al. [27] to assimilate FY-3E MWHS-2 data within the China Meteorological Administration Global Forecast System (CMA_GFS) using a Four-Dimensional Variational (4D-Var) system. Their analysis concluded that FY-3E MWHS-2 radiances significantly benefited the humidity and temperature analysis fields. Moreover, improvements in short-term heavy rain prediction were highlighted as a result of FY-3E MWHS-2 data assimilation. Bi and Zou [28] compared the cloud/rain structures of Typhon Muifa (2022) by all-sky simulations of FY-3E MWHS-2 observations at channel 15. They found that the FY-3E MWHS-2 observations showed a significant symmetric component in the eyewall and inner core of Muifa, which are better captured by the GFS all-sky simulations than the ERA-5 all-sky simulations. They also pointed out that FY-3E MWHS-2 observations can capture the deep convective systems within Typhoon Muifa, but neither the ERA-5 reanalysis nor the GFS analysis can. Huang et al. [29] studied the impact of assimilating MWHS-2 radiance data using various background fields and rapid radiative transfer models on the analysis and forecast of Super Typhoon Muifa (2022). They discovered that assimilating MWHS-2 radiance data primarily corrects the near-surface wind and sea-level pressure fields simulated with ERA-5 reanalysis data, leading to enhanced typhoon intensity. Chen et al. [30] evaluated the impact of a joint assimilation of MWHS-2 radiances under all-sky conditions from both the FY-3C and FY-3D

satellites on Typhoon Hagupit forecasting within regional areas. By assimilating cloud- and precipitation-affected MWHS-2 observations, the forecasts of Typhoon Hagupit's track, intensity, and associated precipitation were improved.

Although previous studies have highlighted the improvements in short-term forecasts due to the assimilation of MWHS-2 data from FY series satellites, the independent and combined impacts of FY-3D MWHS-2, FY-3E MWHS-2, and conventional data assimilation on typhoons are less evaluated. Additionally, the impact of different assimilation strategies for both conventional and satellite data on forecasting still seems uncertain. The objective of this study is to assess the influence of both FY-3D and FY-3E MWHS-2 observation assimilation and different assimilation strategies on the analysis and forecast accuracy in the context of typhoon prediction. To be specific, the single and combined impacts of FY-3D MWHS-2, FY-3E MWHS-2, and conventional observations are assessed for Typhoon Muifa in 2022. In addition, data assimilation strategies are evaluated in terms of assimilating both conventional and satellite data simultaneously, as well as the sequential assimilation of conventional observations and satellite data.

The subsequent sections of this study are structured as follows: Section 2 provides an overview of the 3D-Var method within the Weather Research and Forecasting Data Assimilation (WRFDA) system, along with the datasets used in this study. In Section 3, the typhoon Muifa (2022) and the experimental design are introduced. Section 4 presents the analysis and forecast results. Finally, Sections 5 and 6 contain the discussions and conclusions, respectively.

2. Material and Methods

2.1. WRFDA System

The experiments in this study utilized the Weather Research and Forecasting Model (WRF) (v 4.4) along with its 3D-Var data assimilation system, designed and developed by the National Center for Atmospheric Research (NCAR) [31]. The system includes various assimilation methods, such as 3D-Var, 4D-Var, and hybrid assimilation. In this study, the traditional 3D-Var method was employed. As a starting point, the 3D-Var method was chosen due to its computational efficiency and technological maturity. To attain the optimal estimate of the atmospheric state, the 3D-Var assimilation method minimizes the cost function through iteration. Through iterative minimization of a predefined cost function, this method facilitates the attainment of an optimal analysis of the atmospheric state. The cost function is listed as,

$$\mathbf{J}(\mathbf{x}) = (\mathbf{x} - \mathbf{x_b})^{\mathbf{T}}\mathbf{B}^{-\mathbf{1}}(\mathbf{x} - \mathbf{x_b}) + [\mathbf{y_0} - \boldsymbol{H}(\mathbf{x})]^{\mathbf{T}}\mathbf{R}^{-1}[\mathbf{y_0} - \boldsymbol{H}(\mathbf{x})] \quad (1)$$

where $\mathbf{x}$ denotes the state vector representing the model's state, which is the analysis after the minimization. $\mathbf{x_b}$ stands for the background field, typically derived from prior information such as historical observations or model outputs. $\mathbf{B}$ denotes the background error covariance matrix, encapsulating uncertainties associated with the background field. The background error covariance matrix was calculated using the National Meteorological Center (NMC) method [32] by calculating the differences in the 24 h and 12 h forecasts for one month during 1 August to 30 August 2022. The horizontal correlations were estimated between grid points of each field using the NMC method as a function of distance. A Gaussian curve, as described in [33] is then fitted to the data to provide correlation length scales for use in the recursive filter algorithm. It is found that the magnitudes of the length scales are rather similar to those in the previous studies [34,35]. $\boldsymbol{H}(\mathbf{x})$ denotes the observation operator, which utilizes the Community Radiative Transfer Model (CRTM) model to map the model state to the observation space. $\mathbf{y}_0$ represents the vector of observed data. $\mathbf{R}$ is the observation error covariance matrix, describing the error properties of the observed data. The first term in the cost function accounts for the contribution of model background error, quantifying the discrepancy between the model output and the background field. Conversely, the second term captures the contribution of observation error, measuring the disparity between the model output and the observed data.

Minimization of the cost function facilitates the determination of the optimal state vector **x**, thereby achieving an optimal alignment between model output and observational data.

2.2. Quality Control and Bias Correction

Quality control (QC) of radiance data is a crucial process in satellite data assimilation that ensures the accuracy and reliability of the data for use in weather forecasting models. Referring to the previous study by Chen et al. [30] Xian et al. [36], the quality control scheme adopted is as follows:

(1) remove the radiance data with TBs lower than 50 K or higher than 550 K;
(2) remove radiance data over mixed surface types;
(3) remove the radiance data if the bias-corrected normalized first-guess departure (OMB) exceeded 3σ, where σ represents the specified standard deviation of the observation errors;
(4) remove the radiance data if the difference between observation and background simulated light temperature is more than 15 K;
(5) removes radiances with CLWP ≥ 0.2 kg/m^2 calculated from the background.

After the quality control, the systematic bias of the satellite data must also be corrected. The CRTM observation operator is used in this study. The bias of radiance observations can be expressed as a linear combination of several predictors:

$$\widetilde{\boldsymbol{H}}(\mathbf{x}, \boldsymbol{\beta}) = \boldsymbol{H}(\mathbf{x}) + \boldsymbol{\beta_0} + \sum_{i=1}^{N_p} \boldsymbol{\beta_i} \mathbf{p_i}\,, \tag{2}$$

where **x** represents the model state vector, $\boldsymbol{H}(\mathbf{x})$ is the observation operator before bias correction, and $\widetilde{\boldsymbol{H}}(\mathbf{x}, \boldsymbol{\beta})$ is the observation operator after bias correction. $\boldsymbol{\beta_0}$ is the constant part of the total bias, $\boldsymbol{\beta_i}$ and $\mathbf{p_i}$ represent the **ith** predictor and the bias correction coefficients, respectively, and are assumed to be channel-dependent. The bias correction coefficient $\boldsymbol{\beta_i}$ can be estimated offline through the variational bias correction method, which is called variational bias correction (VarBC) [37,38]. Furthermore, a thinning setting with a spacing of 54 km was applied to the MWHS-2 radiance data in this study.

2.3. Data Usage

In this study, conventional observation data were acquired from diverse sources through the Global Telecommunications System (GTS), encompassing radiosonde observations, aircraft reports, surface observations, and atmospheric motion vectors. The China Land Data Assimilation System's (CLDAS) multi-source precipitation fusion dataset was utilized for the verification of precipitation forecasts. This dataset provides hourly precipitation analysis with a spatial resolution of $0.0625^\circ \times 0.0625^\circ$. It can describe the influence of terrain changes on temperature and precipitation, and it also reasonably represents the spatial distribution of precipitation in China [39–42]. The assessment of track and intensity predictions involved the utilization of the best track data for Typhoon Muifa, sourced from the Tropical Cyclone Data Center of the China Meteorological Administration (CMA) via https://tcdata.typhoon.org.cn/zjljsjj.html, accessed on 20 September 2023. These best track records serve as a reliable benchmark for evaluating the performance of typhoon forecasting models, characterized by precise spatial coordinates (latitude and longitude), maximum wind speed (MWS), and minimum sea level pressure (MSLP), among other parameters. Furthermore, the fifth-generation ECMWF reanalysis dataset (ERA-5) was employed as the background field, which is widely used in other studies [27,28,43–46]. With a spatial resolution of $0.25^\circ \times 0.25^\circ$, ERA-5 provides a comprehensive and high-resolution compilation of atmospheric parameters globally, encompassing variables such as temperature, humidity, wind, pressure, and precipitation.

The MWHS-2 instruments onboard the FY-3D and FY-3E provide 15 detection channels, with 4 channels situated near the oxygen absorption line at 118.75 GHz specifically allocated for vertical atmospheric temperature profiling. Additionally, five channels near the water vapor absorption line at 183.31 GHz are utilized to capture finer details of atmospheric water

vapor vertical distribution [24]. Furthermore, both satellites have two window channels designated for precipitation detection at 89 GHz and 150 GHz (FY-3D) or 166 GHz (FY-3E). However, a notable distinction between the FY-3D and FY-3E MWHS-2 instruments lies in the latter's enhancement. The FY-3E MWHS-2 introduces an advancement by adjusting the detection frequency in the 150 GHz window region to 166 GHz. This modification aims to elevate instrument radiometric calibration precision and detection sensitivity, thereby enhancing the overall performance of the MWHS-2 instrument onboard the FY-3E satellite. Thus, while maintaining core similarities in MWHS-2 configuration and operational principles, the FY-3E satellite integrates an upgraded feature to augment its functionality and efficacy. Furthermore, five channels from the MWHS-2 instrument are utilized to discern the vertical distribution of humidity within the atmosphere. In this study, the assimilation of radiance was constrained to channels 11, 12, 13, 14, and 15, as determined by the information provided in Table 1 regarding the characteristics of FY-3D and FY-3E MWHS-2's different channels. These specific channels are selected based on their sensitivity to different atmospheric layers and their ability to provide complementary information for accurate humidity retrieval. By focusing on these channels, the assimilation system is expected to effectively utilize MWHS-2 observations to improve the representation of atmospheric moisture profiles in the NWP models.

Table 1. Properties of the FY-3D and FY-3E MWHS-2 channels. V and H represent the vertical and horizontal polarization, respectively.

Channel	Central Frequency (GHZ) (FY-3D)	Central Frequency (GHz) (FY-3E)	Polarizations	Resolution (km)	Bandwidth (MHz)	Main Sensitivity
1	89		H	30	1500	Surface
2	118.75 ± 0.08		V	30	20	Temperature
3	118.75 ± 0.2		V	30	100	Temperature
4	118.75 ± 0.3		V	30	165	Temperature
5	118.75 ± 0.8		V	30	200	Temperature
6	118.75 ± 1.1		V	30	200	Temperature
7	118.75 ± 2.5		V	30	200	Temperature
8	118.75 ± 3.0		V	30	1000	Temperature
9	118.75 ± 5.0		V	30	2000	Temperature
10	150	166	H	15	1500	Surface
11	183.31 ± 1		V	15	500	Humidity
12	183.31 ± 1.8		V	15	700	Humidity
13	183.31 ± 3		V	15	100	Humidity
14	183.31 ± 4.5		V	15	2000	Humidity
15	183.31 ± 7		V	15	2000	Humidity

3. Typhoon Case and Experimental Design

3.1. Overview of Typhoon Muifa

On 6 September 2022, Typhoon Muifa originated in the northwest Pacific Ocean with an initial pressure of 1002 hPa. During its development, Muifa significantly impacted regions including mainland China, Taiwan, and Japan (Figure 1). Following its formation, the typhoon rapidly intensified, undergoing multiple fluctuations in intensity throughout its landfall process. Notably, Muifa made four landfalls along the coast of China, which was an uncommon occurrence since 1949 and the first recorded instance of a typhoon landfall in northeastern China. The typhoon's effects were widespread, particularly felt in the Yangtze River Delta region, and prompted emergency measures such as railway closures and passenger train suspensions. The main affected regions included Zhejiang Province, Shanghai, Jiangsu, and Shandong Province. Specifically, Muifa first made landfall at 1230 UTC on 14 September 2022 along the coastal areas of Putuo, Zhoushan, and Zhejiang Province, nearly reaching the level of a severe typhoon. With wind speeds of 40 m/s and a central pressure of 965 hPa, it marked one of the highest intensities of a typhoon's landfall that occurred in China in 2022. Subsequently, it made a second landfall at 1630 UTC on

15 September 2022 in Fengxian, Shanghai, with a strength reaching the level of a typhoon and setting a record for the strongest typhoon to land in Shanghai in nearly 70 years. Later, Muifa made its third landfall along the coastal areas of Laoshan, Qingdao, and Shandong Province at 1600 UTC on 16 September 2022, and was then downgraded to a tropical storm. Finally, at 0440 UTC on 16 September 2022, it made its fourth landfall in Jinpu New District, Dalian, Liaoning Province, by which time it had weakened to an extratropical cyclone. The CMA ceased its numbering of the typhoon at 1200 UTC on 16 September 2022.

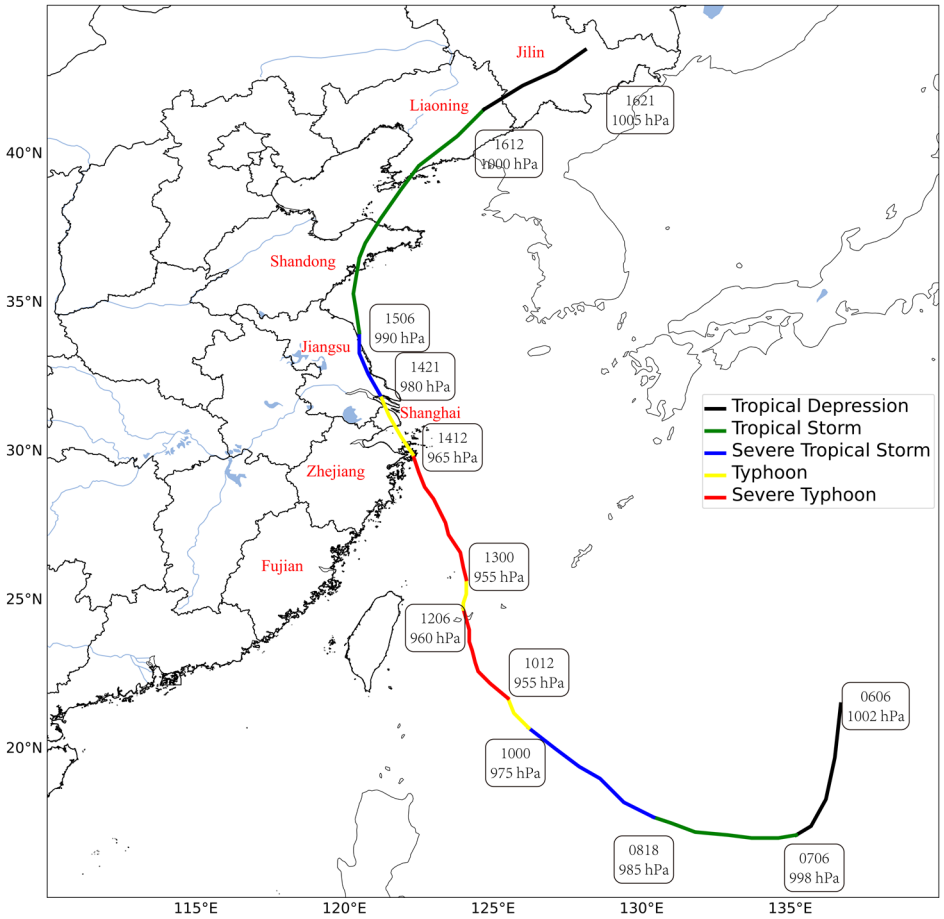

Figure 1. The evolution of Typhoon Muifa's intensity levels throughout its track, recorded from 0600 on 6 September to 2100 on 16 September UTC. Time (day and hour) and central pressure of typhoon are noted at nodes where the typhoon intensity shifts.

3.2. Experimental Design

The Advanced Research Weather Research and Forecasting (ARW-WRF) model, version 4.4, was utilized in this study. Figure 2 shows the simulation domain centered at (31°N, 123°E), with a horizontal grid spacing of 9 km covering the domain (559 × 469 points). Vertically, the domain was divided into 61 layers, with 10 hPa at the top. The initial and boundary conditions of the model were derived from the 0.5° × 0.5° ERA-5 data. The CV5 scheme is employed for the background error covariance matrix **B**. The model adopts various physical parameterization schemes, including the WRF Single-Moment 6-Class Microphysics (WSM6) scheme [47], the Yonsei University (YSU) boundary layer scheme [48], the Dudhia short-wave radiation scheme [49], the Rapid Radiative Transfer Model (RRTM) longwave radiation scheme [50], the Noah land-surface model land-surface scheme, and the Kain–Fritsch cumulus parameterization scheme [51].

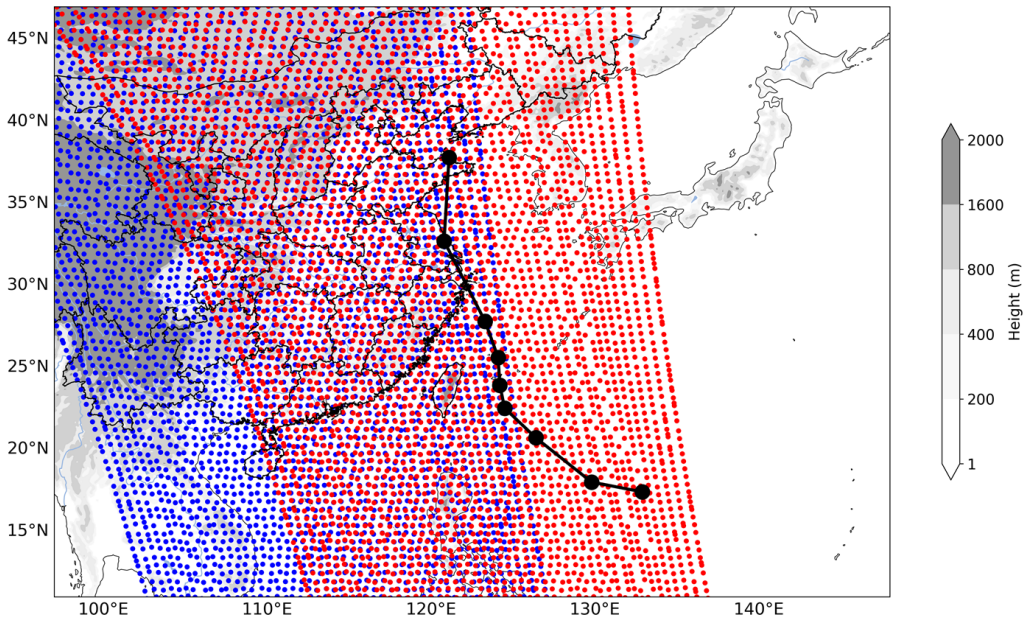

Figure 2. Terrain height (filled colors, unit: m) and the best track of Typhoon Muifa 24 h interval (black dot), from 0000 UTC on 8 September to 0000 UTC 16 September within the model domain. Blue points represent FY-3D MWHS-2 data, while red points represent FY-3E MWHS-2 data.

Six parallel experimental configurations were established to assess the implications of assimilating various satellite data, including FY-3D MWHS-2 and FY-3E MWHS-2, along with conventional GTS data (Figure 3). Furthermore, the study also investigates the consequential impacts of the different strategies for simultaneously assimilating conventional data and satellite data on the NWP. The six experiments, denoted as CTRL, GTS_DA, 3D_DA, 3E_DA, 3D_R_DA, and 3E_R_DA, were conducted for the case. The simulations in the experiments span from 0000 UTC on 14 September to 0000 UTC on 16 September 2022. The CTRL experiment does not assimilate any observation, which serves as the baseline with the initial and lateral boundary conditions derived from the ERA-5 reanalysis. In data assimilation experiments, the initial background fields originated from a 6 h spin-up forecast initialized at 0000 UTC on 14 September. The GTS_DA experiment involved the assimilation of conventional observations sourced from the NCEP operational GTS dataset at 0600 UTC on 14 September. In the 3D_DA experiment, both the GTS and the FY-3D MWHS-2 data are assimilated simultaneously at 0600 UTC on 14 September. Employing a two-step assimilation approach, in the 3D_R_DA experiment, the conventional observations are assimilated before adopting the radiances in the second step at 0600 UTC on 14 September. Each data assimilation in the above experiments is followed by 42 h deterministic forecasts from on 14 September to 0600 UTC on 16 September 2022. In terms of the DA experiments with FY-3E MWHS-2 observations, in the 3E_DA experiment, the GTS data are assimilated at 0600 UTC on 14 September followed by a 3 h forecast until 0900 UTC on the same day. At 0900 UTC on 14 September, both GTS data and FY-3E MWHS-2 data were assimilated at 0900 UTC on 14 September. The 3E_R_DA experiment is similar to the 3E_DA experiment, except GTS and FY-3E MWHS-2 data are assimilated in two steps. Each data assimilation in the above experiments with FY-3E MWHS-2 data are followed by 39 h deterministic forecasts from on 14 September to 0900 UTC on 16 September 2022.

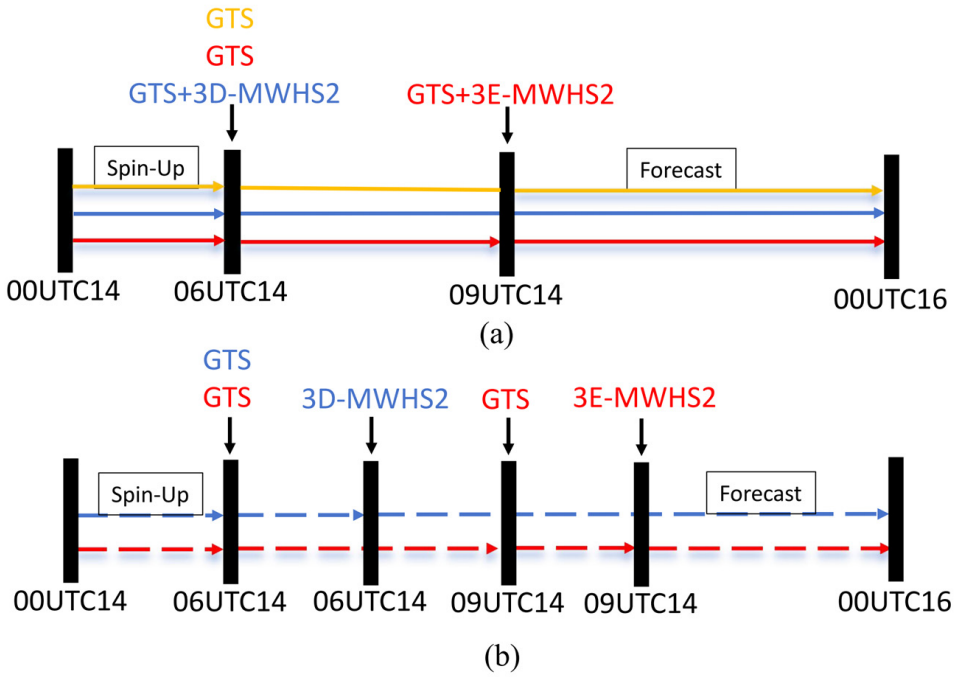

Figure 3. The flow chart for the data assimilation experiments. One-step experiments including GTS_DA (yellow solid line), 3D_DA (blue solid line), and 3E_DA (red solid line) are depicted in (**a**), two-step experiments including 3D_R_DA (blue dashed line) and 3E_R_DA (red dashed line) are depicted in (**b**).

4. Results

4.1. Radiance Simulations and Bias Correction

Inherent systematic biases in satellite data have the potential to substantially degrade the quality of both analysis and forecast fields; therefore, it is essential to conduct rigorous quality control and bias correction procedures. The observed brightness temperature was sourced from the MWHS-2 dataset following quality control and bias correction. The background brightness temperature was generated from the simulations with the forward radiative transfer model CRTM, which utilized the background before the assimilation as the input. In contrast, the simulated brightness temperature of the analysis was derived from the brightness temperature simulated with CRTM using the analysis after the data assimilation. Figure 4 shows the observed brightness temperature minus the background brightness temperature (OMB) and the observed brightness temperature minus the simulated brightness temperature of the analysis (OMA) following bias correction for FY-3D MWHS-2 at 0600 UTC and FY-3E MWHS-2 at 0900 UTC, along with the mean, standard deviation (stdv), and root mean square (rms). The statistics are calculated based on the data from all the locations with MWHS-2 observations across the entire domain at this time, as shown in Figures 4 and 5. FY-3E data near the typhoon center were removed as part of the quality control procedure, as the scanning swath passed directly through the center of the typhoon. Before assimilating MWHS-2 radiance data, the absolute values of most scan points' OMB indicate significant differences between the background field and observations. The absolute values of OMA approach 0 K for most of the observations after the data assimilation, indicating the effectiveness of assimilation.

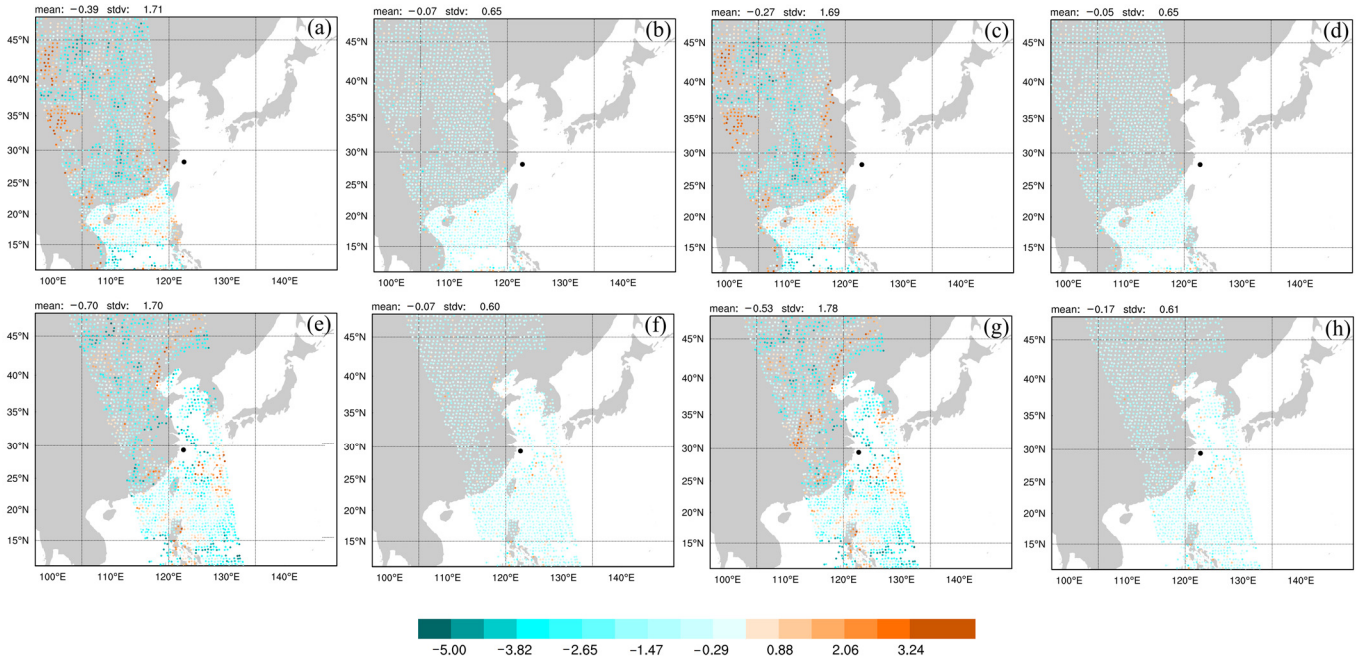

Figure 4. OMB of (**a**) 3D_DA, (**c**) 3D_R_DA, (**e**) 3E_DA, and (**g**) 3E_R_DA; OMA of (**b**) 3D_DA, (**d**) 3D_R_DA, (**f**) 3E_DA, and (**h**) 3E_R_DA for the brightness temperature (units: K) of channel 11. The blue dot and red dot represent the location of the typhoon center at 0600 UTC on 14 September 2022 and 0900 UTC on 14 September 2022, respectively.

Figure 5 presents a comparison of scatter distributions depicting the differences between OMB and OMA in the context of different data assimilation experiments. Before the bias correction, the observed and background brightness temperatures displayed a wide dispersion. As expected, the scatter plot between observed and analyzed brightness temperature tends to converge closer to the diagonal line, accompanied by a reduction in standard deviation after the bias correction. After the data assimilation, the scatter plots of the analyzed brightness temperature (Figure 5c,f,i,l) further fit the diagonal line compared to the background field. The mean, stdv, and root mean square error (RMSE) are further reduced and converging to 0 K, indicating the effectiveness of assimilating MWHS-2 radiance data. Specifically, both the OMB and the mean before assimilation exhibited smaller values compared to one-step assimilation methods. This reduction is likely attributed to the initial step's impact, which effectively reduced systemic bias. RMSE and stdv in the 3D_DA (Figure 5a–c) have shown a decline compared to the 3D_R_DA (Figure 5d–f), signifying an enhanced alignment with observational data. The lack of reduction in RMSE and stdv observed in 3E_R_DA (Figure 5j–l) when compared to 3E_DA (Figure 5g–i) could be due to the two-step assimilation strategy, which might have increased the utilization of FY-3E MWHS-2 satellite data, thereby affecting the assimilation process. In summary, the resulting analyses exhibit smaller errors, markedly superior to the background field. Furthermore, the scatter plot after assimilation converges more closely to the diagonal line, indicating the benefit of assimilating MWHS-2 data.

Figure 6 presents the results of four radiance data assimilation experiments, including the number of assimilated satellite data, mean, and stdv. These experiments were conducted to assess the performance of the two satellite radiances in the assimilation system, as well as the effects of different data assimilation approaches in terms of applying conventional and radiance observations on the results. In terms of the data quantity (Figure 6a), it is noted that the one-step and two-step data assimilation approaches have a relatively smaller impact on the data count for FY-3D MWHS-2. In channel 11, the observed data counts are 1956 and 1961 for one-step assimilation and two-step assimilation, respectively. Whereas, for FY-3E MWHS-2, the number of assimilated satellite data increases significantly

in two-step assimilation compared to one-step assimilation. This indicates that two-step assimilation may affect data quality control and indirectly influence the absorption of satellite data. Regarding the mean (Figure 6b,c) and stdv (Figure 6d,e), no significant difference is observed between the 3D_DA and 3D_R_DA experiments, but some disparities are evident in the 3E_DA and 3E_R_DA experiments. Specifically, the mean of OMA displays some fluctuations, with 3E_DA outperforming 3E_R_DA experiments in channels 11, 12, and 13. OMB before and after bias correction also show some differences, with two-step assimilation generally resulting in better results both before and after bias correction. As for the stdv, the 3E_DA experiment is significantly smaller than that of the 3E_R_DA experiment, indicating larger discrepancies between the values simulated by the 3E_R_DA experiment and their mean value.

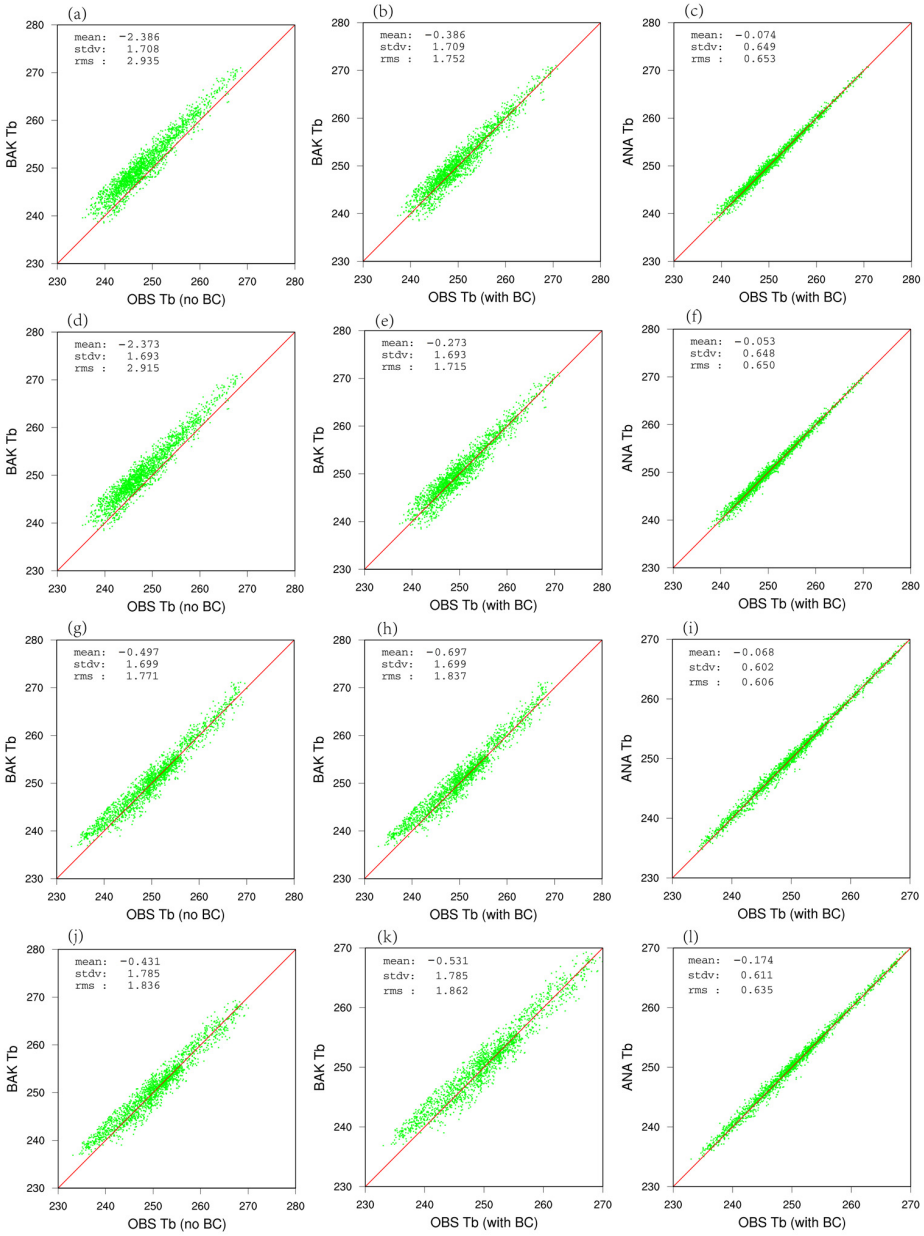

Figure 5. Scatter distribution of the brightness temperature (unit: K) of channel 11 simulated from (**a**,**d**,**g**,**j**) the background before the bias correction, (**b**,**e**,**h**,**k**) the background after bias correction, and (**c**,**f**,**i**,**l**) the analysis after the bias correction in the y-axis versus the observed radiances in the x-axis. (**a**–**c**) 3D_DA experiment, (**d**–**f**) 3D_R_DA experiment, (**g**–**i**) 3E_DA experiment, and (**j**–**l**) 3E_R_DA experiment.

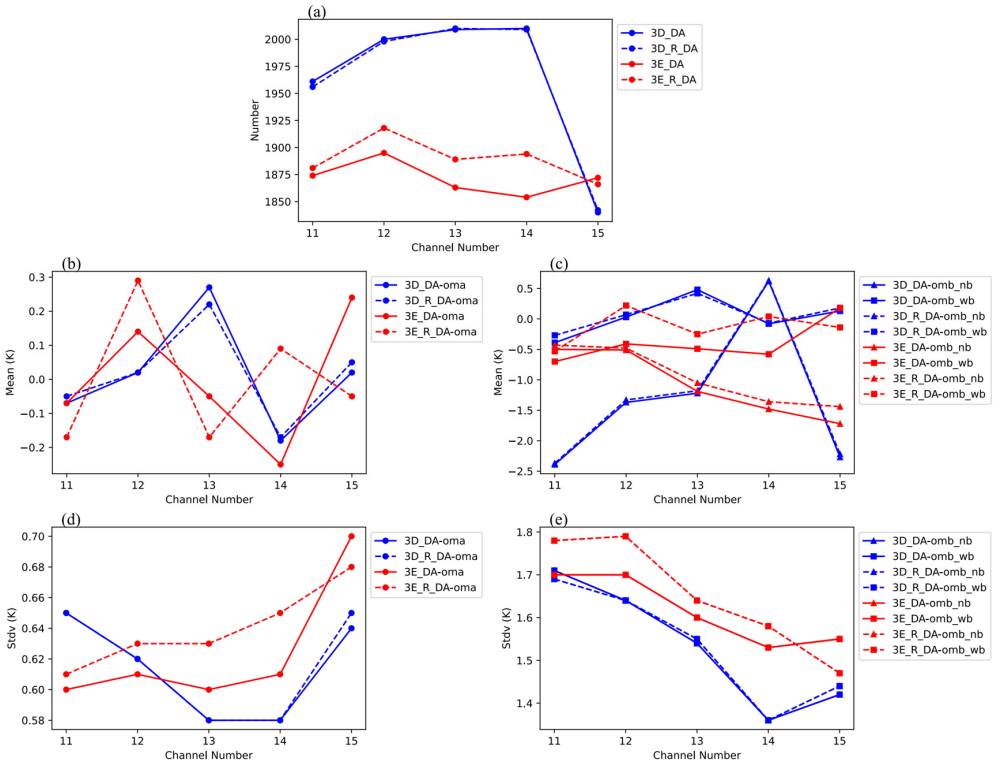

Figure 6. (**a**) The number of assimilated satellite data for the experiment; (**b**,**c**) Mean for the experiment and (**d**,**e**) stdv for the experiment.

4.2. Typhoon Structure Analysis

4.2.1. Analysis of the Thermal Structures

Water vapor is crucial for the occurrence, enhancement, and maintenance of tropical cyclones. Figure 7 shows the difference between the analysis and background fields of 500 hPa water vapor mixing ratio and wind speed. The label "First Step" in Figure 7c,f illustrates the effect of initially assimilating GTS data on the background within the context of a two-step assimilation strategy. While the label "Second Step" in Figure 7e,h depicts the additional impact of assimilating MWHS-2 data subsequent to GTS assimilation. The combined influence resulting from the assimilation of both datasets is demonstrated in the label "Two-Steps" in Figure 7f,i. In the GTS_DA experiment (Figure 7a), predominantly positive differences are observed, with only small negative differences ranging from -2 g/kg to 0 g/kg being evident for the northeast of the typhoon. In the one-step assimilation, small positive differences ranging from 0 g/kg to 2 g/kg are noted in the east of the typhoon in the 3D_DA experiment (Figure 7b), while negative differences are observed in the west, particularly in the southwest, with values ranging from -8 g/kg to -10 g/kg. In the 3E_DA experiment (Figure 7c), predominantly positive differences are found around the typhoon, with a notable magnitude of up to 10 g/kg along with notable negative differences ranging from -8 g/kg to -10 g/kg, in the southwest of the typhoon. Regarding the two-step assimilation experiments, positive differences are observed after assimilating GTS data in the first step of the 3D_R_DA experiment (Figure 7d), with minimal difference compared to the GTS_DA experiment. Subsequent assimilation of MWHS-2 data in the second step reinforces the negative differences in the southwest caused by the first step, and negative differences are observed in other areas as well. For the 3E_R_DA experiment (Figure 7g), assimilation of GTS data enhances the positive differences in the northwest of the typhoon in the first step, while small negative differences are observed in the southwest. Similarly, significant positive differences are reinforced in the north and southeast after assimilation of MWHS-2 data in the second step, along with the increase in negative differences in the southwest. Overall, it can be seen that the water vapor mixing ratio differences obtained

after two-step assimilation from the 3D_R_DA experiment exhibit minimal differences compared to the results from the 3D_DA experiment. Conversely, the 3E_R_DA experiment predominantly exhibits widespread positive differences in the northern typhoon and localized negative differences in the southwest and southeast, slightly more pronounced compared to those in the 3E_DA experiment.

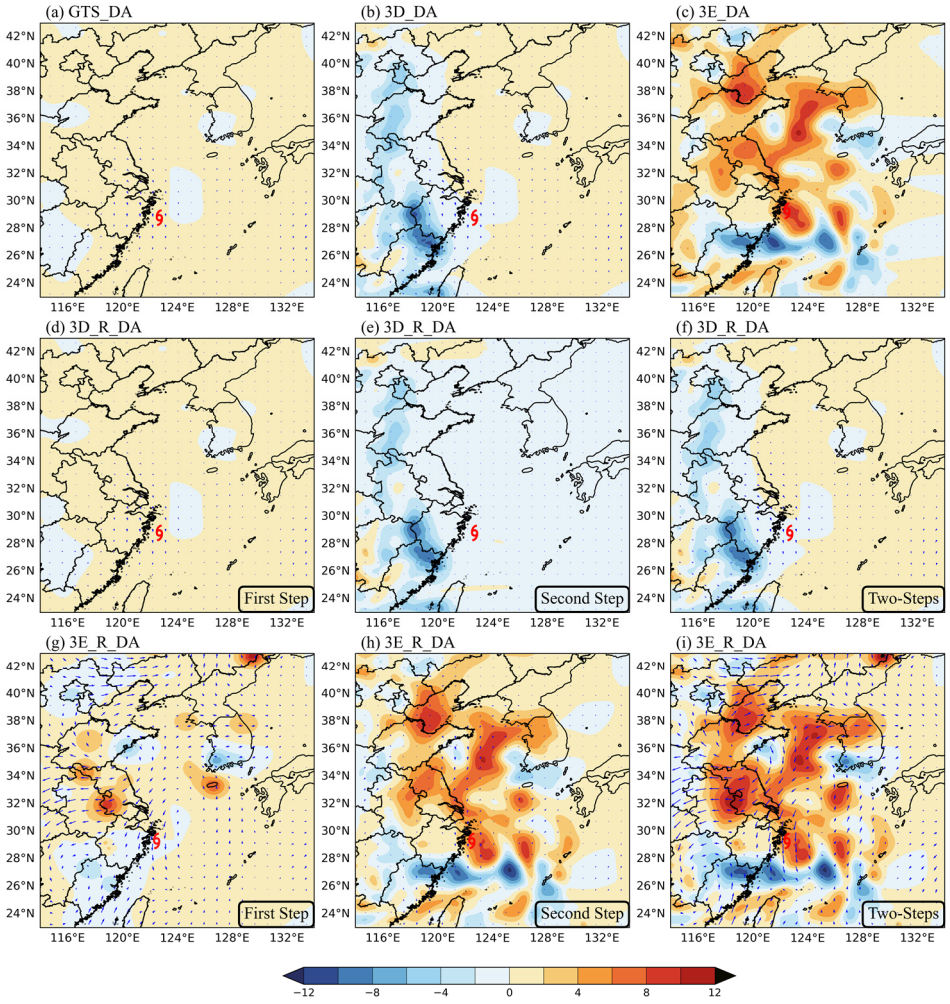

Figure 7. The 500 hPa water vapor mixing ratio differences (analysis minus background, shading, unit: g/kg) and wind speed (vector, unit: m/s) for (**a**) GTS_DA, (**b**) 3D_DA, and (**c**) 3E_DA. The differences in the (**d**) first step, (**e**) second step, and (**f**) two-steps in 3D_R_DA at 0600 UTC 14 September. The differences in the (**g**) first step, (**h**) second step, and (**i**) two-steps in 3E_R_DA at 0900 UTC 14 September. The red symbol represents the position of the typhoon sourced from the CMA at 0600 UTC 14 September (**a**,**b**,**d**–**f**) and 0900 UTC 14 September (**c**,**g**–**i**).

To assess the effect of assimilation experiments, Figure 8 presents the temperature differences at 500 hPa for the assimilation experiments. Notably, negative temperature increments are observed surrounding the typhoon in the GTS_DA experiment (Figure 8a), while positive differences are also evident in both the 3D_DA and 3E_DA experiments (Figure 8b,c). In terms of the two-step assimilation, negative temperature differences are found around the typhoon following the assimilation of GTS data in the first step within the 3D_R_DA experiment (Figure 8d–f). As pointed out by Li et al. [52], physically, the strengthened typhoon vortex circulation should be accompanied by the warming of the typhoon core. The assimilation of MWHS-2 data in the second step effectively corrects the negative differences induced by the assimilation of GTS data in the first step, resulting in positive temperature differences in the typhoon center. Similarly, positive temperature

differences are observed around the typhoon after the assimilation of GTS data in the first step of the 3E_R_DA experiment (Figure 8g–i). The assimilation of MWHS-2 data in the second step further enhances these positive differences. Moreover, the negative differences observed in the GTS_DA experiment imply possible shortcomings in accurately representing the warm-core structure essential for intensification. Conversely, the observed positive differences in both the 3D_DA and 3E_DA experiments suggest that assimilating MWHS-2 data contributes to the formation of warm core structures within typhoons and shows a more realistic representation of these structures, thereby facilitating their development and intensity maintenance. In addition, the results from the two-step assimilation experiment reveal an enhancement of positive differences around the typhoon center after MWHS-2 assimilation, further strengthening the warm-core structure. Additionally, these enhancements correct the temperature discrepancies from the initial assimilation of GTS data, leading to a more precise portrayal of the typhoon's thermodynamic structure.

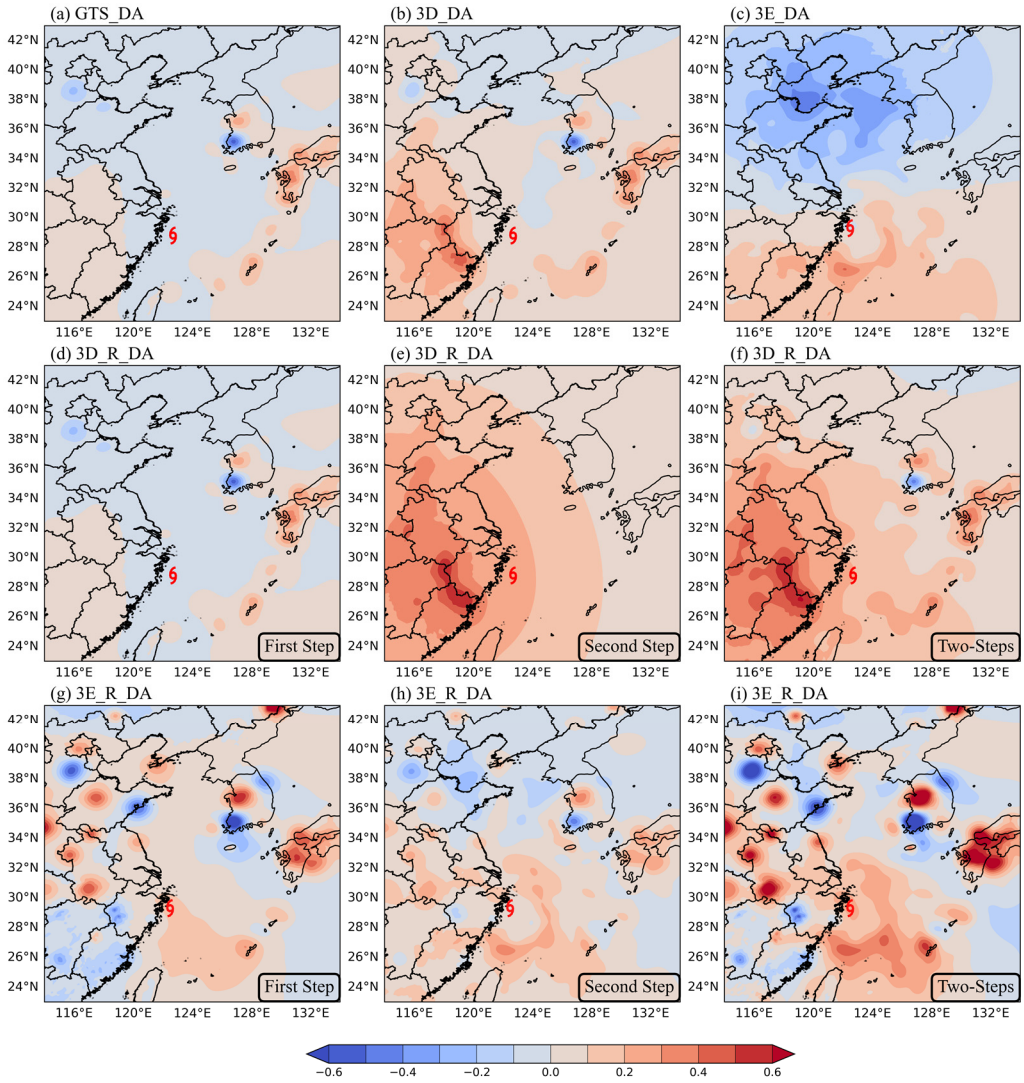

Figure 8. Same as Figure 7, but for the temperature (unit: K).

4.2.2. The 500 hPa Geopotential Height

The geopotential height and geopotential height difference at 500 hPa between the analysis and the background are displayed in Figure 9. It is pointed out that the change in geopotential height is able to correct the location of the typhoon in Wang et al. [53]. The GTS_DA experiment (Figure 9a) and the 3D_DA experiment (Figure 9b) reveal an increase in geopotential height to the west of the typhoon center and a corresponding

decrease to the northeast. And an increase in height is evident surrounding the typhoon in the 3E_DA experiment (Figure 9c), with relatively greater differences observed in the north. Consequently, both the GTS_DA and 3D_DA experiments exhibit a northwestward trend, while the 3E_DA experiment demonstrates a slight northward shift, leading the predicted track to fit more closely with the best track illustrated in Figure 9. In terms of the 3D_R_DA experiment (Figure 9d–f), assimilation of GTS data in the first step results in an increase in geopotential height in the westward direction of the typhoon center along with a decrease in the northeast. After assimilating MWHS-2 data in the second step, the negative differences in the northeast were corrected, and it also enhanced the positive differences surrounding the typhoon. In the case of the 3E_R_DA experiment, a notable decrease is observed in Figure 9g in the geopotential height surrounding the typhoon following the assimilation of GTS data in the first step, which is particularly evident in the western and northeastern. Subsequent assimilation of MWHS-2 data in the second step results in a decrease in geopotential height in the northeastern part of the typhoon and minor positive differences in the northwest based on the assimilation of GTS data in the first step. The combined two-step assimilation of the 3E_R_DA experiment exhibits a noticeable decrease northeastward of the typhoon and a slight decrease to the west, thereby influencing the typhoon track more towards the northwest compared to the 3D_R_DA experiment.

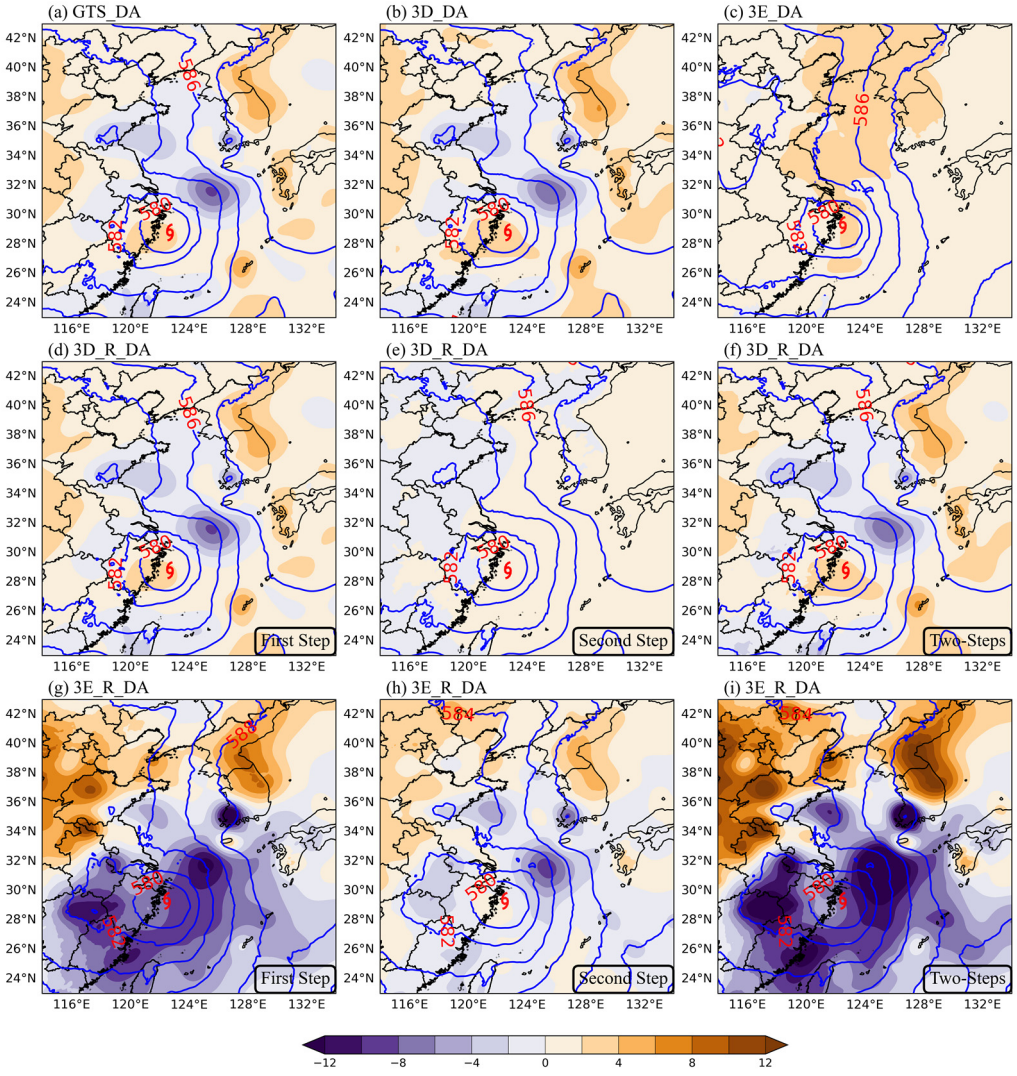

Figure 9. Same as Figure 7, but for geopotential height (contours, units: $m^2\ s^{-2}$; contours every 2 $m^2\ s^{-2}$) and geopotential height differences (analysis minus background, shading, unit: m).

4.3. Forecast Performance

To provide a comprehensive assessment of the impact of six experiments on the forecast accuracy, sounding and surface synoptic (SYNOP) observations are used as the reference for the comparative analysis. Figure 10 displays the RMSE of the u-wind (meridional wind), v-wind (zonal wind), temperature, and specific humidity at 1200 UTC on 15 September 2022 along with the significance level above 95% denoted with dots. It can be seen that MWHS-2 DA experiments have demonstrated lower RMSE over the GTS_DA and CTRL experiments at the lower layers (700–1000 hPa) for the wind, particularly for v-wind within the 400–900 hPa layers. While the RMSEs are comparable for two-step and one-step assimilation strategies in FY-3D MWHS-2 DA experiments for wind field simulation, the two-step assimilation strategy involving the FY-3E MWHS-2 dataset generally outperforms the one-step approach for both the u-wind and v-wind. Specifically, this advantage is evident for u-wind at pressure levels ranging from 700 hPa to 400 hPa and from 300 hPa to 150 hPa, and for v-wind from 700 hPa to 300 hPa. In terms of the RMSE of temperature and specific humidity, the MWHS-2 DA experiments exhibit a lower RMSE compared to the GTS_DA and CTRL at the lower layer. Similarly, the difference in RMSE between two-step and one-step assimilation strategies in FY-3D MWHS-2 DA experiments is not significant for the temperature or specific humidity. However, the two-step assimilation strategy in the FY-3E MWHS-2 DA experiments shows a lower RMSE for temperature from 400 hPa to 100 hPa and for specific humidity from 600 hPa to 300 hPa. The majority of the color dots have passed the significance test. However, in certain areas, the results are not significant, primarily due to the insufficient observational data. Specifically regarding the specific humidity, significant positive differences are found in the middle and upper layers, whereas they are not significant when closer to the surface. It should be pointed out that the reduced significance of surface humidity might be due to the concentration of humidity information, which increases the difficulty of making further improvements.

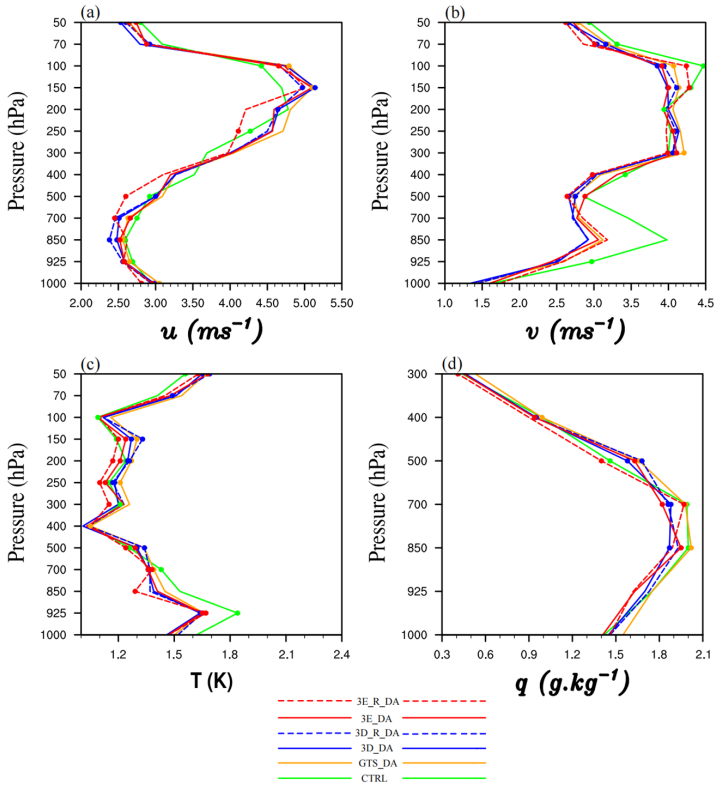

Figure 10. RMSE vertical profiles of (**a**) u-wind (m/s), (**b**) v-wind (m/s), (**c**) temperature (K), and (**d**) specific humidity (g/kg) forecasts versus sounding and surface synoptic (SYNOP) observations at 1200 UTC on 15 September 2022. Error dots indicate statistical significance at the 95% confidence level.

Figure 11 illustrates the best track and the track predictions for the 39 h, along with the track errors. The best track data are from the CMA [54]. In addition, the values of the track error at each time are shown in Table 2. In the 39 h deterministic forecasts, the performance of typhoon track prediction was assessed across six experiments. The averaged track error in the CTRL experiment was 137.73 km. The GTS_DA experiment demonstrated a reduction in the averaged track error to 120.54 km. The track forecasts are further improved after assimilating the MWHS-2 radiance data, with an averaged track error of 117.22 km for 3D_DA, 107.17 km for 3E_DA, 102.62 km for 3D_R_DA, and 115.34 km for 3E_R_DA, respectively. It seems that the track error is the smallest from CTRL for the first 24 h. It can probably be explained by the fact that starting the simulation at the beginning of the same day the typhoon made landfall makes it more challenging to demonstrate the impact of data assimilation. This is because the model already provides a well-simulated typhoon system in the control experiment. However, a significant deviation in the track of the CTRL experiment occurred after the first 24 h, which may be caused by the typhoon landfall. The track deviation is corrected successfully by the data assimilation experiments after the multi-variables are balanced after 24 h. Both the 3D_DA and 3E_DA experiments demonstrated comparable performance in the first 18 h (1409 UCT to 1503 UTC) of forecasting. From 18 to 30 h, the track errors in 3D_DA and 3E_DA are rather comparable. Yet, during the 33 to 39 h period, the averaged track error in 3E_DA is 94.51 km smaller compared to that of 3D_DA. It can be found that the two-step data assimilation method is able to further improve the track forecast, especially for the later forecast hours (Figure 11b). These results indicate that over the entire forecast period, the 3D_R_DA experiment exhibited the best performance in terms of the typhoon track prediction, followed by the 3E_DA experiment.

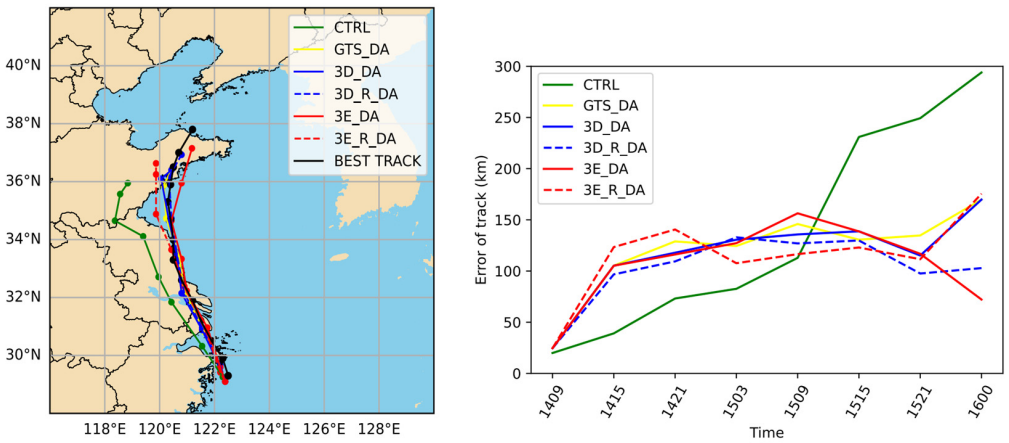

Figure 11. (**a**) Typhoon Muifa's track from 0900 UTC on 14 September to 0000 UTC on 16 September 2022 and (**b**) the corresponding track error, the numbers on the x-axis represent day and hour, respectively.

Table 2. The track error (km) of six experiments during simulation.

DayHour	1409	1415	1421	1503	1509	1515	1521	1600	Average
CTRL	19.93	39.10	73.16	82.63	112.86	230.95	249.27	293.96	137.73
GTS_DA	24.61	105.21	128.95	124.44	145.93	130.62	134.74	169.78	120.54
3D_DA	24.61	105.21	117.89	130.60	135.74	138.79	115.14	169.78	117.22
3D_R_DA	24.61	96.74	109.41	132.93	126.98	129.84	97.58	102.85	102.62
3E_DA	24.61	105.21	116.18	127.23	156.39	138.71	116.86	72.16	107.17
3E_R_DA	24.61	123.40	140.57	107.64	116.50	122.98	111.53	175.48	115.34

MSLP and maximum surface wind speed (MSWS) are two critical meteorological parameters that directly reflect the intensity and developmental trends of typhoons. MSLP and MSWS errors at specific time points are detailed in Tables 3 and 4, respectively. In Figure 12, it can be seen that the errors of MSLP and MSWS between the control and assimilation experiments are comparable within the first 24 h. Starting the simulation at the beginning of the same day when the typhoon made its landfall makes it more challenging to show the impact of data assimilation since the model provides a well-simulated typhoon system in the control experiment. However, the assimilation experiments exhibit better performance compared to the control experiment after the first 24 h. In terms of MSLP errors (Figure 12a), the CTRL experiment displays the highest average error at 11.71 hPa, and the 3E_R_DA experiment demonstrates the most favorable performance within the assimilation experiments, showcasing the lowest average error at 9.97 hPa, followed by the 3E_DA experiment at 10.46 hPa, and the 3D_DA and 3D_R_DA experiments at 11.07 hPa and 10.62 hPa, respectively. For the error of MSWS (Figure 12b), the highest average error is −9.60 m/s in the CTRL experiment. The 3E_R_DA experiment demonstrates the lowest average error at −7.88 m/s, followed by the 3D_R_DA experiment at −8.18 m/s, with the 3E_DA and 3D_DA experiments at −8.28 m/s and −8.45 m/s, respectively. It is evident that the 3E_R_DA experiment performs the best for simulating both MSLP and MSWS. Moreover, the two-step assimilation methods exhibit superior performance in simulating MSLP and MSWS compared to the one-step assimilation methods. The two-step assimilation method is able to more accurately capture the complex variations during typhoon development and promptly adjust the model state in situations of rapid typhoon intensification or weakening, thereby enhancing the accuracy of simulation results.

Table 3. MSLP error (hPa) of six experiments during simulation.

DayHour	1409	1415	1421	1503	1509	1515	1521	1600	Average
CTRL	35.06	23.97	11.63	4.85	2.97	3.77	5.13	6.30	11.71
GTS_DA	36.98	25.06	12.49	4.56	1.53	2.54	2.31	3.02	11.06
3D_DA	37.0	25.15	12.56	4.66	1.68	2.82	1.88	2.84	11.07
3D_R_DA	37.26	23.32	12.41	4.54	1.60	2.03	1.72	2.07	10.62
3E_DA	37.08	24.41	11.17	3.67	0.79	1.53	2.32	2.75	10.46
3E_R_DA	36.63	24.24	11.26	4.25	0.56	0.61	1.01	1.20	9.97

Table 4. The MSWS error (m/s) of six experiments during simulation.

DayHour	1409	1415	1421	1503	1509	1515	1521	1600	Average
CTRL	−18.29	−18.29	−9.70	−5.93	−5.06	−5.74	−6.83	−6.95	−9.60
GTS_DA	−18.67	−18.09	−9.33	−6.26	−4.05	−4.44	−4.30	−4.05	−8.65
3D_DA	−18.73	−18.38	−9.32	−5.96	−4.58	−4.15	−3.79	−2.72	−8.45
3D_R_DA	−18.77	−18.54	−9.18	−6.48	−4.08	−3.88	−2.74	−1.77	−8.18
3E_DA	−18.64	−17.17	−9.16	−6.10	−4.29	−4.37	−3.73	−2.80	−8.28
3E_R_DA	−18.64	−19.1	−10.17	−4.21	−3.95	−3.91	−1.90	−1.16	−7.88

To assess the impact of assimilating MWHS-2 data on the structural characteristics of Typhoon Muifa, Figure 13 depicts the vertical cross-section of wind speed and potential temperature at the core of Typhoon Muifa at 0900 UTC on 15 September 2022. It can be found that assimilation experiments exhibit a more upright eyewall and a narrower typhoon eye compared to that in the control experiment. The typhoon structure in the 3D_DA experiment (Figure 13c) is rather comparable to that in the GTS_DA (Figure 13b). Regarding the two-step assimilation experiment, for the FY-3D MWHS-2, the 3D_R_DA experiment (Figure 13d) outperforms the 3D_DA experiment by improving the distribution of the typhoon eye and eyewall. Similarly, the 3E_R_DA experiment (Figure 13f) yields a typhoon eye that is narrower compared to the 3E_DA experiment. In summary, the data assimilation experiments yielded more enhanced structures of the typhoon than

the CTRL experiment (Figure 13a) did. Moreover, the two-step assimilation experiments have the potential to further improve the structure of typhoons compared to one-step assimilation experiments.

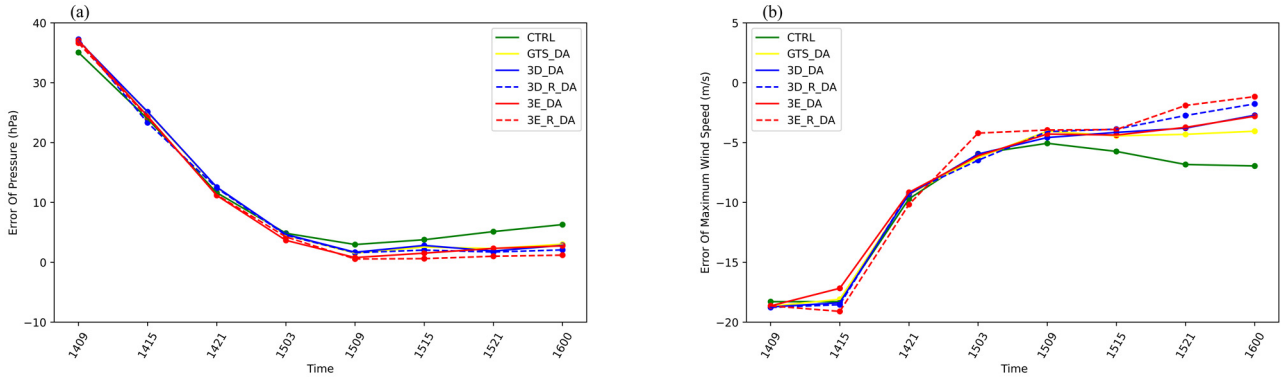

Figure 12. The 39 h forecast errors of (**a**) MSLP (unit: hPa) and (**b**) MSWS (unit: m/s), initialized at 0900 UTC on 14 September 2022.

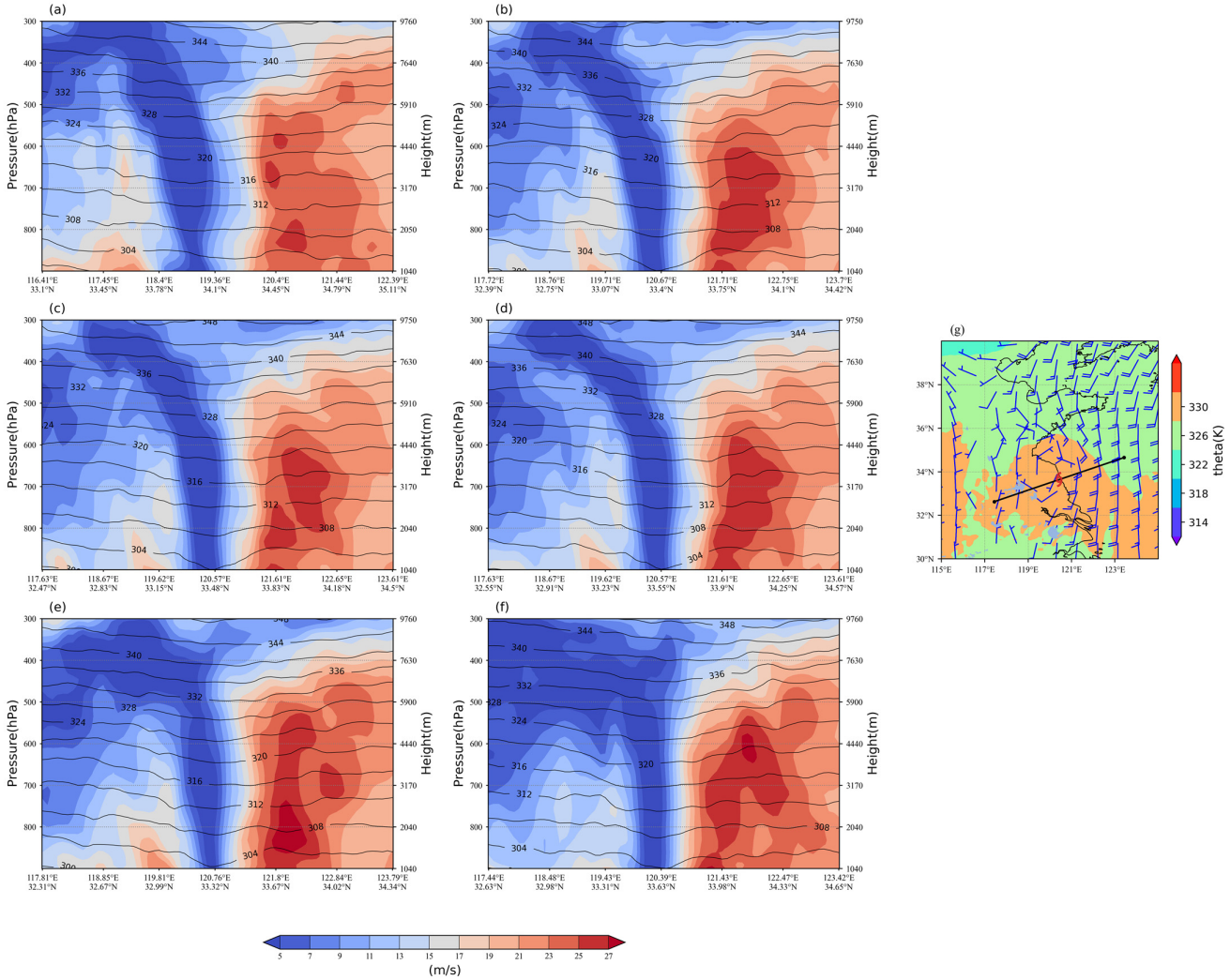

Figure 13. The vertical cross section of the wind speed (shading, unit: m/s) and potential temperature (contours, unit: K, intervals of 4 K) for (**a**) CTRL, (**b**) GTS_DA, (**c**) 3D_DA, and (**d**) 3D_R_DA at 0600 UTC 14 September, (**e**) 3E_DA, and (**f**) 3E_R_DA at 0900 UTC 14 September. (**g**) is the cross section with the wind speed (blue wind barbs, unit: m/s) and potential temperature (shading, unit: K). The red symbol is the position of the typhoon at 0600 UTC 14 September.

The multi-source precipitation fusion dataset from the CLDAS was employed as an observation to verify the accuracy of precipitation forecasts. Due to the constraints imposed by data availability, the absence of observational data over oceanic surfaces precludes the validation of accumulated precipitation over these regions. Consequently, this study focuses exclusively on the analysis of terrestrial precipitation patterns. Figure 14 shows the 24 h accumulated precipitation from 0900 UTC on 14 September to 0900 UTC on 15 September 2022 for the six experiments, along with the observation. From Figure 14g, it can be observed that precipitation primarily occurs at locations A and B. It can be seen that all six experiments exhibited obvious occurrences of significant false precipitation when the accumulated precipitation exceeded 100 mm. However, they provided a relatively accurate representation of the general range and distribution of the rain belt, traversing the regions of East China and Northeast China. At location A, precipitation in all six experiments exhibited a westward bias relative to the observations. Notably, the rain belts in the CTRL (Figure 14a) and 3E_R_DA (Figure 14f) experiments appeared disconnected, resulting in a more accurate representation of the precipitation distribution at this location. Moreover, the CTRL experiment experienced instances of underreporting at location B, while the assimilation experiment showed a closer match with the observational data. Overall, the 3E_R_DA experiment provided a superior portrayal of both the position and intensity of precipitation compared to the other experiments.

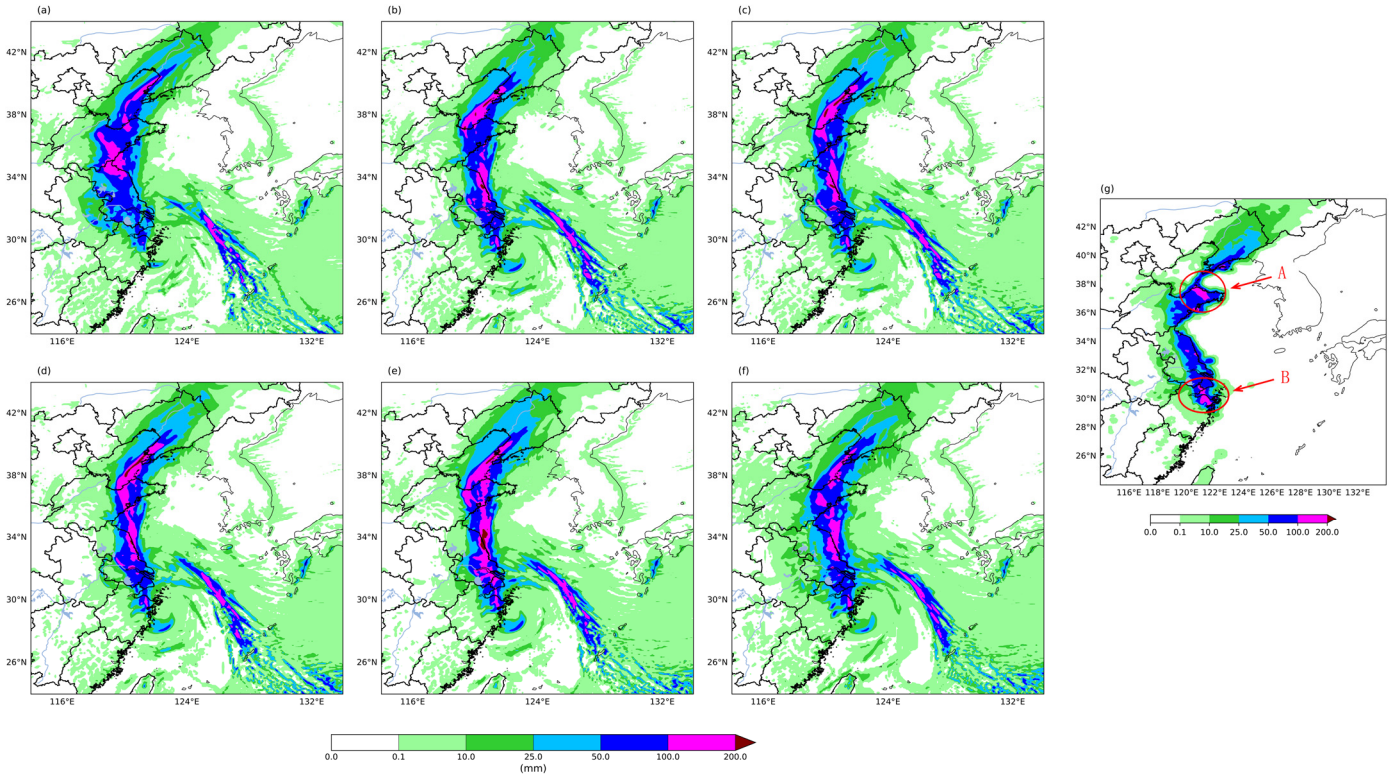

Figure 14. The 24 h accumulated precipitation distribution (unit: mm) from 0900 UTC on 14 September to 0900 UTC on 15 September in the experiments (**a**) CTRL, (**b**) GTS_DA, (**c**) 3D_DA, (**d**) 3D_R_DA, (**e**) 3E_DA, (**f**) 3E_R_DA, and in (**g**) the observation.

To quantitatively assess the effectiveness of the precipitation forecast skill across the six experiments, the Equitable Threat Score (ETS) is employed. The ETS is calculated as follows [55]:

$$\mathrm{ETS} = \frac{\mathrm{hits} - \mathrm{hits}_{\mathrm{rand}}}{\mathrm{hits} + \mathrm{misses} + \mathrm{false}_{\mathrm{alarms}} - \mathrm{hits}_{\mathrm{rand}}}, \quad (3)$$

$$\text{hits}_{\text{rand}} = \frac{(\text{hits} + \text{misses}) * (\text{hits} + \text{false}_{\text{alarms}})}{\text{hits} + \text{misses} + \text{false}_{\text{alarms}} + \text{correct}_{\text{negatives}}}. \quad (4)$$

The term hits represents the instances where both the observed and predicted values exceed a predefined threshold, signifying accurate identification of event occurrences. Conversely, the misses describe situations where the observed value exceeds the threshold while the predicted value falls below it, indicating a failure to anticipate genuine events. The $\text{false}_{\text{alarms}}$ represent situations where the prediction exceeds the threshold while the observed value does not, indicating erroneous predictions of event occurrences, and the $\text{correct}_{\text{negatives}}$ signify cases where both observed and predictions are below the threshold, indicating correct predictions of event absence. The $\text{hits}_{\text{rand}}$ serves as a baseline score, estimating the expected number of hits under random predictions. The ETS varies from -1 to 1. The highest value of ETS is 1, indicating a perfect rainfall forecast.

Figure 15 displays the ETS for the 24 h accumulated precipitation across six experiments from 0900 UTC on 14 September to 0900 UTC on 15 September 2022. The scores for 3D_DA, 3D_R_DA, and 3E_DA exhibit comparable performance across different rainfall thresholds. Notably, the ETS values in the 3E_R_DA experiment exceed those of other experiments for rainfall thresholds between 10 and 100 mm. A comparison between one-step and two-step assimilation reveals similar performance between 3D_R_DA and 3D_DA. Significant differences are noted between the 3E_DA and 3E_R_DA experiments, with the 3E_R_DA experiment exhibiting higher scores.

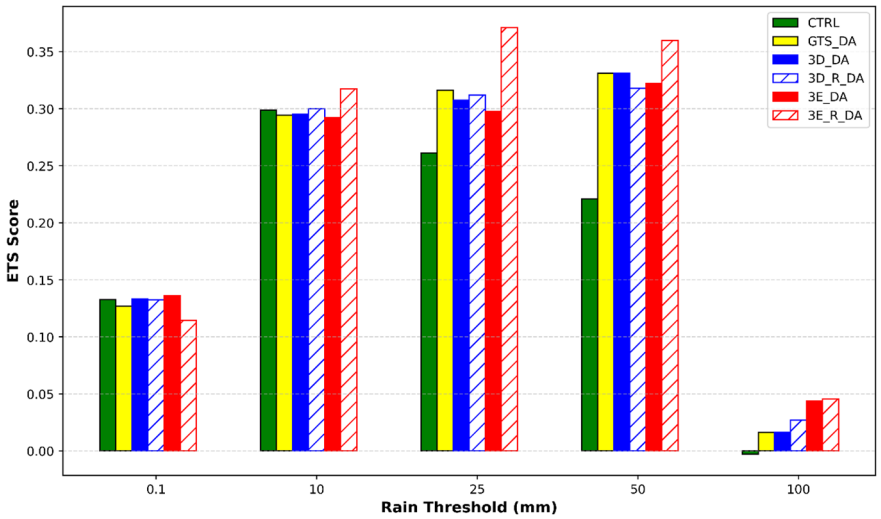

Figure 15. ETS of 24 h accumulated precipitation at different thresholds.

5. Discussions

The impact of MWHS-2 radiance data from FY-3D and FY-3E on the analyses and forecasts of typhoon Muifa (2022) is assessed using the regional WRF model along with its 3D-Var systems under clear-sky conditions in this study. In addition, the data assimilation strategies are studied in terms of applying conventional and radiance observations to determine the impact of the sequence of assimilating conventional and MWHS-2 radiance data. It was found that a notable decrease in errors was observed in the analyses compared to the background after assimilating MWHS-2 data, confirming the effectiveness of bias correction and assimilation. Additionally, assimilating clear-sky MWHS-2 radiance data leads to beneficial adjustments in the geopotential height and temperature fields around the typhoon center compared to only assimilating GTS data, which may contribute to the track improvement from the radiance assimilation experiment. The assimilation of MWHS-2 radiance data has resulted in improvements in the dynamic and thermal structures of typhoons by providing valuable humidity information, yielding more significant improvements over the assimilation of GTS data. By assimilating GTS data at first, the

large-scale atmospheric conditions are better refined since GTS data provides conventional observation data worldwide. Based on this, the subsequent assimilation of satellite data can further adjust the model state, which is crucial for enhancing the accuracy of typhoon forecasts. The assimilation of FY-3E MWHS-2 radiances demonstrated superior performance in simulating the MSLP and the MSWS than FY-3D MWHS-2 did, with average errors of 10.46 hPa (versus 11.07 hPa) in the MSLP and −8.28 m/s (versus −8.45 m/s) in the MSWS. Additionally, two-step assimilation methods demonstrate superiority over one-step assimilation methods in terms of simulating MSLP and MSWS. Furthermore, the two-step assimilation yields generally higher ETS for the precipitation. Specifically, 3E_R_DA exhibits the most favorable precipitation distribution and generally the highest ETS among all the experiments. The above outcomes suggest that appropriate strategies are of great importance in combining multi-source observations for TC forecasts.

6. Conclusions

In this study, the results are promising in terms of assimilating MWHS-2 radiance data from FY-3D and FY-3E into the analyses and forecasts of Typhoon Muifa (2022). The results of the experiments also indicate that two-step assimilation has a positive effect on the analysis and prediction of Typhoon Muifa. The assimilation of MWHS-2 data from FY-3D and FY-3E enhances the thermal and dynamic structures of typhoons. Specifically, FY-3E demonstrates significant advantages in simulating MSLP and MSWS and exhibits better performance in the ETS for precipitation. In addition, the radiances from the FY-3E MWHS-2 have improved the representation of the typhoon's structure with a more upright eyewall and a narrower typhoon eye. For the experiments assimilating MWHS-2 data from the FY-3D and FY-3E satellites, two-step assimilation yields better simulations of MSLP and MSWS compared to one-step assimilation. The improved simulation capabilities are particularly notable in the detailed depiction of the thermal and dynamic characteristics of typhoons. Additionally, the ETS for the two-step assimilation outperforms that of the one-step assimilation. Furthermore, the quantity of satellite data assimilated shows a significant difference between two-step and one-step assimilation, particularly in experiments related to the FY-3E MWHS-2. This suggests that two-step assimilation may impact data quality control and could indirectly affect satellite data assimilation.

While the assimilation of MWHS-2 in FY-3D and FY-3E has yielded promising results in the typhoon simulation, it also presents certain limitations in the forecast accuracy of the precipitation and TC intensity that require further improvements in other aspects. These aspects include configuring more suitable physical parameterizations, optimizing the model domain and resolution to reduce model errors, using additional data sources such as radar data, conducting cycling data assimilation schemes, and enhancing the background error estimation processes. In a future study, all-sky radiance MWHS-2 observations will also be applied to better utilize the cloud-affected MWHS-2 radiance observations. The development of methodologies for assimilating surface observations is also planned to further introduce MWHS-2 observations from surface-sensitive channels. Additionally, the utilization of 4D-Var, hybrid-Var, or other advanced assimilation methods will also be considered, as they are expected to enhance the accuracy of the typhoon prediction with the MWHS-2 radiance data.

Author Contributions: Conceptualization, F.S. and H.L.; writing—original draft, X.Y.; writing—review and editing, F.S. and D.X.; formal analysis, J.L., X.Y., F.S., D.X. and A.S.; data curation, L.H. and X.Y. All authors have read and agreed to the published version of the manuscript.

Funding: This research was funded by the National Natural Science Foundation of China (G42192553), Open Fund of State Key Laboratory of Remote Sensing Science (OFSLRSS202321), Program of Shanghai Academic/Technology Research Leader (21XD1404500), the Shanghai Typhoon Research Foundation (TFJJ202107), Open Grants of the State Key Laboratory of Severe Weather (2024LASW-B13), Open Fund of Fujian Key Laboratory of Severe Weather and Key Laboratory of Straits Severe Weather (2023KFKT03), and China Meteorological Administration Tornado Key Laboratory (TKL202306).

Data Availability Statement: The FY-3D and FY-3E all-sky MWHS-2 data were freely downloaded from http://satellite.nsmc.org.cn, accessed on 10 September 2023, along with the conventional observations from National Centers for Environmental Prediction (NCEP) operational Global Telecommunication System (GTS) from http://rda.ucar.edu/datasets/ds337.0/, accessed on 10 September 2023. Part of the software was associated with the National Center for Atmospheric Research (NCAR) using the version 4.4 of WRF and WRF-3DVar system. The analysis is provided by the fifth generation of the European Centre for Medium-Range Weather Forecasts (ECMWF) reanalysis (ERA-5) data with a horizontal resolution of $0.25^\circ \times 0.25^\circ$, available at https://cds.climate.copernicus.eu/cdsapp#!/, accessed on 15 August 2023. Figures were made with NCL version 6.6.2 from https://www.ncl.ucar.edu and Python version 3.3.8 from https://www.python.org, accessed on 5 November 2023.

Acknowledgments: We acknowledge the High Performance Computing Center of Nanjing University of Information Science & Technology for their support of this work.

Conflicts of Interest: The authors declare no conflicts of interest.

References

1. Saunders, R. The use of satellite data in numerical weather prediction. *Weather* **2021**, *76*, 95–97. [CrossRef]
2. Eyre, J.R.; Bell, W.; Cotton, J.; English, S.J.; Forsythe, M.; Healy, S.B.; Pavelin, E.G. Assimilation of satellite data in numerical weather prediction. Part II: Recent years. *Q. J. R. Meteorol. Soc.* **2022**, *743*, 521–556. [CrossRef]
3. Eyre, J.R.; English, J.S.; Forsythe, M. Assimilation of satellite data in numerical weather prediction. Part I: The early years. *Q. J. R. Meteorol. Soc.* **2020**, *146*, 49–68. [CrossRef]
4. Xu, D.; Liu, Z.; Huang, X.Y.; Min, J.; Wang, H. Impact of Assimilating IASI Radiance Observations on Forecasts of Two Tropical Cyclones. *Meteorol. Atmos. Phys.* **2013**, *122*, 1–18. [CrossRef]
5. Collard, A.; Hilton, F.; Forsythe, M.; Candy, B. From Observations to Forecasts-Part 8: The use of satellite observations in numerical weather prediction. *Weather* **2011**, *66*, 31–36. [CrossRef]
6. Balsamo, G.; Agusti-Panareda, A.; Albergel, C.; Arduini, G.; Beljaars, A.; Bidlot, J.; Blyth, E.; Bousserez, N.; Boussetta, S.; Brown, A.; et al. Satellite and In Situ Observations for Advancing Global Earth Surface Modelling: A Review. *Remote Sens.* **2018**, *10*, 2038. [CrossRef]
7. Zapotocny, T.H.; Jung, J.A.; Le Marshall, J.F.; Treadon, R.E. A two-season impact study of satellite and in situ data in the NCEP Global Data Assimilation System. *Weather Forecast.* **2007**, *22*, 887–909. [CrossRef]
8. Errico, R.M.; Ohring, G.; Weng, F.; Bauer, P.; Ferrier, B.; Mahfouf, J.F.; Turk, J. Assimilation of Satellite Cloud and Precipitation Observations in Numerical Weather Prediction Models: Introduction to the JAS Special Collection. *J. Atmos. Sci.* **2007**, *64*, 3737–3741. [CrossRef]
9. Xu, D.; Shu, A.; Shen, F. Effects of Clear-Sky Assimilation of GPM Microwave Imager on the Analysis and Forecast of Typhoon "Chan-Hom". *Sensors* **2020**, *20*, 2674. [CrossRef]
10. Xu, D.; Shen, F.; Min, J. Assimilation of GPM Microwave Imager Radiance for Track Prediction of Typhoon Cases with the WRF Hybrid En3DVAR System. *Adv. Atmos. Sci.* **2021**, *38*, 983–993. [CrossRef]
11. Duncan, D.I.; Bormann, N.; Hólm, E.V. On the addition of microwave sounders and numerical weather prediction skill. *Q. J. R. Meteorol. Soc.* **2021**, *147*, 3703–3718. [CrossRef]
12. Rosenkranz, P.W.; Komichak, M.J.; Staelin, D.H. A Method for Estimation of Atmospheric Water Vapor Profiles by Microwave Radiometry. *J. Appl. Meteorol. Climatol.* **1982**, *21*, 1364–1370. [CrossRef]
13. Liu, Q.; Cao, C.; Grassotti, C.; Lee, Y.K. How Can Microwave Observations at 23.8 GHz Help in Acquiring Water Vapor in the Atmosphere over Land? *Remote Sens.* **2021**, *13*, 489. [CrossRef]
14. Shen, F.; Min, J. Assimilating AMSU-A Radiance Data with the WRF Hybrid En3DVAR System for Track Predictions of Typhoon Megi (2010). *Adv. Atmos. Sci.* **2015**, *32*, 1231–1243. [CrossRef]
15. Choudhury, D.; Gupta, A.; Rani, S.I.; George, J.P. Impact of SAPHIR radiances on the simulation of tropical cyclones over the Bay of Bengal using NCMRWF hybrid-4DVAR assimilation and forecast system. *J. Earth Syst. Sci.* **2020**, *129*, 209. [CrossRef]
16. Dhanya, M.; Gopalakrishnan, D.; Chandrasekar, A.; Singh, S.K.; Prasad, V. The impact of assimilating Megha Tropiques SAPHIR radiances in the simulation of tropical cyclones over the Bay of Bengal using the WRF model. *Int. J. Remote Sens.* **2016**, *37*, 3086–3103. [CrossRef]
17. Xie, Y.; Chen, M.; Shi, J.; Fan, S.; He, J.; Dou, Y. Impacts of Assimilating ATMS Radiances on Heavy Rainfall Forecast in RMAPS-ST. *Remote Sens.* **2020**, *12*, 1147. [CrossRef]
18. Lai, Z.; Peng, S. The Effect of Assimilating AMSU-A Radiance Data from Satellites and Large-Scale Flows from GFS on Improving Tropical Cyclone Track Forecast. *Atmosphere* **2022**, *13*, 1988. [CrossRef]
19. Dong, C.; Yang, J.; Zhang, W.; Yang, Z.; Lu, N.; Shi, J.; Zhang, P.; Liu, Y.; Cai, B. An Overview of a New Chinese Weather Satellite FY-3A. *Bull. Am. Meteorol. Soc.* **2009**, *90*, 1531–1544. [CrossRef]
20. Zhang, P.; Lu, Q.; Hu, X.; Gu, S.; Yang, L.; Min, M.; Chen, L.; Xu, N.; Sun, L.; Bai, W.; et al. Latest progress of the Chinese meteorological satellite program and core data processing technologies. *Adv. Atmos. Sci.* **2019**, *36*, 1027–1045. [CrossRef]

21. Zhang, P.; Hu, X.; Lu, Q.; Zhu, A.; Lin, M.; Sun, L.; Chen, L. FY-3E: The first operational meteorological satellite mission in an early morning orbit. *Adv. Atmos. Sci.* **2022**, *39*, 1–8. [CrossRef]
22. Duncan, D.I.; Bormann, N. *On the Addition of Microwave Sounders and NWP Skill, Including Assessment of FY-3D Sounders*; European Centre for Medium-Range Weather Forecasts: Reading, UK, 2020.
23. Carminati, F.; Migliorini, S. All-sky data assimilation of MWTS-2 and MWHS-2 in the Met Office global NWP system. *Adv. Atmos. Sci.* **2021**, *38*, 1682–1694. [CrossRef]
24. Carminati, F.; Atkinson, N.; Candy, B.; Lu, Q. Insights into the Microwave Instruments Onboard the Fengyun 3D Satellite: Data Quality and Assimilation in the Met Office NWP System. *Adv. Atmos. Sci.* **2021**, *38*, 1379–1396. [CrossRef]
25. Bormann, N.; Duncan, D.; English, S.; Healy, S.; Lonitz, K.; Chen, K.; Lawrence, H.; Lu, Q. Growing Operational Use of FY-3 Data in the ECMWF System. *Adv. Atmos. Sci.* **2021**, *38*, 1285–1298. [CrossRef]
26. Xu, D.; Shu, A.; Li, H.; Shen, F.; Min, J. Effects of Assimilating Clear-Sky FY-3D MWHS2 Radiance on the Numerical Simulation of Typhoon Ampil. *Remote Sens.* **2021**, *13*, 2873. [CrossRef]
27. Xiao, H.; Han, W.; Zhang, P.; Bai, Y. Assimilation of data from the MWHS-II onboard the first early morning satellite FY-3E into the CMA global 4D-Var system. *Meteorol. Appl.* **2023**, *30*, e2133. [CrossRef]
28. Bi, M.; Zou, X. Comparison of Cloud/Rain Band Structures of Typhoon Muifa (2022) Revealed in FY-3E MWHS-2 Observations with All-Sky Simulations. *J. Geophys. Res.* **2023**, *128*, e2023JD039410. [CrossRef]
29. Huang, L.; Xu, D.; Li, H.; Jiang, L.; Shu, A. Assimilating FY-3D MWHS2 Radiance Data to Predict Typhoon Muifa Based on Different Initial Background Conditions and Fast Radiative Transfer Models. *Remote Sens.* **2023**, *15*, 3220. [CrossRef]
30. Chen, K.; Chen, Z.; Xian, Z.; Li, G. Impacts of the All-Sky Assimilation of FY-3C and FY-3D MWHS-2 Radiances on Analyses and Forecasts of Typhoon Hagupit. *Remote Sens.* **2023**, *15*, 2279. [CrossRef]
31. Barker, D.; Huang, X.Y.; Liu, Z.; Auligné, T.; Zhang, X.; Rugg, S.; Ajjaji, R.; Bourgeois, A.; Bray, J.; Chen, Y.; et al. The weather research and forecasting model's community variational/ensemble data assimilation system: WRFDA. *Bull. Am. Meteorol. Soc.* **2012**, *93*, 831–843. [CrossRef]
32. Parrish, D.F.; Derber, J.C. The National Meteorological Center's spectral statistical-interpolation analysis system. *Mon. Weather Rev.* **1992**, *120*, 1747–1763. [CrossRef]
33. Barker, D.M.; Huang, W.; Guo, Y.R.; Bourgeois, A.J.; Xiao, Q.N. A three-dimensional variational data assimilation system for MM5: Implementation and initial results. *Mon. Weather Rev.* **2004**, *132*, 897–914. [CrossRef]
34. Shen, F.; Song, L.; Li, H.; He, Z.; Xu, D. Effects of different momentum control variables in radar data assimilation on the analysis and forecast of strong convective systems under the background of northeast cold vortex. *Atmos. Res.* **2022**, *280*, 106415. [CrossRef]
35. Sun, J.; Wang, H.; Tong, W.; Zhang, Y.; Lin, C.-Y.; Xu, D. Comparison of the impacts of momentum control variables on high-resolution variational data assimilation and precipitation forecasting. *Mon. Weather Rev.* **2016**, *144*, 149–169. [CrossRef]
36. Xian, Z.; Chen, K.; Zhu, J. All-sky assimilation of the MWHS-2 observations and evaluation the impacts on the analyses and forecasts of binary typhoons. *J. Geophys. Res.* **2019**, *124*, 6359–6378. [CrossRef]
37. Derber, J.C.; Wu, W.S. The use of TOVS cloud-cleared radiances in the NCEP SSI analysis system. *Mon. Weather Rev.* **1998**, *126*, 2287–2299. [CrossRef]
38. Dee, D.P. Bias and data assimilation. *Q. J. R. Meteorol. Soc.* **2005**, *131*, 3323–3343. [CrossRef]
39. Sun, S.; Shi, C.; Pan, Y.; Bai, L.; Xu, B.; Zhang, T.; Han, S.; Jiang, L. Applicability Assessment of the 1998–2018 CLDAS Multi-Source Precipitation Fusion Dataset over China. *J. Meteorol. Res.* **2020**, *34*, 879–892. [CrossRef]
40. Han, S.; Liu, B.; Shi, C.; Liu, Y.; Qiu, M.; Sun, S. Evaluation of CLDAS and GLDAS Datasets for Near-Surface Air Temperature over Major Land Areas of China. *Sustainability* **2020**, *12*, 4311. [CrossRef]
41. Liu, J.; Shi, C.; Sun, S.; Liang, J.; Yang, Z.-L. Improving Land Surface Hydrological Simulations in China Using CLDAS Meteorological Forcing Data. *J. Meteorol. Res.* **2019**, *33*, 1194–1206. [CrossRef]
42. Dong, Z.; Zhao, Y.; Feng, X.; Liu, S. Applicability assessment of CLDAS temperature and precipitation products in Inner Mongolia. *J. Arid Meteorol.* **2023**, *41*, 811–819.
43. Hersbach, H.; Bell, B.; Berrisford, P.; Hirahara, S.; Horányi, A.; Muñoz-Sabater, J.; Nicolas, J.; Peubey, C.; Radu, R.; Schepers, D.; et al. The ERA5 global reanalysis. *Q. J. R. Meteorol. Soc.* **2020**, *146*, 1999–2049. [CrossRef]
44. Zhu, Y.; Mahajan, R.; Thomas, C.; Groff, D.; Van Delst, P.; Collard, A.; Kleist, D.; Treadon, R.; Derber, J.C. All-Sky Microwave Radiance Assimilation in NCEP's GSI Analysis System. *Mon. Weather Rev.* **2016**, *144*, 4709–4735. [CrossRef]
45. Wilson, A.B.; Bromwich, D.H.; Hines, K.M. Evaluation of Polar WRF forecasts on the Arctic System Reanalysis domain: Surface and upper air analysis. *J. Geophys. Res.* **2011**, *116*, D11. [CrossRef]
46. Li, Z.; Han, W. Impact of HY-2B SMR radiance assimilation on CMA global medium-range weather forecasts. *Q. J. R. Meteorol. Soc.* **2024**, *150*, 937–957. [CrossRef]
47. Hong, S.Y.; Lim, J.O. The WRF single-moment 6-class microphysics scheme (WSM6). *J. Korean Phys. Soc.* **2006**, *42*, 129–151.
48. Hong, S.Y.; Noh, Y.; Dudhia, J. A new vertical diffusion package with an explicit treatment of entrainment processes. *Mon. Weather Rev.* **2006**, *134*, 2318–2341. [CrossRef]
49. Dudhia, J. Numerical study of convection observed during the winter monsoon experiment using a mesoscale two-dimensional model. *J. Atmos. Sci.* **1989**, *46*, 3077–3107. [CrossRef]

50. Mlawer, E.J.; Taubman, S.J.; Brown, P.D.; Iacono, M.J.; Clough, S.A. Radiative transfer for inhomogeneous atmospheres: RRTM, a validated correlated-k model for the longwave. *J. Geophys. Res. Atmos.* **1997**, *102*, 16663–16682. [CrossRef]
51. Kain, J.S. The Kain–Fritsch convective parameterization: An update. *J. Appl. Meteorol.* **2004**, *43*, 170–181. [CrossRef]
52. Li, Y.; Wang, X.; Xue, M. Assimilation of radar radial velocity data with the WRF ensemble-3DVAR hybrid system for the prediction of hurricane Ike (2008). *Mon. Weather Rev.* **2012**, *140*, 3507–3524. [CrossRef]
53. Wang, X. Application of the WRF hybrid ETKF-3DVAR data assimilation system for hurricane track forecasts. *Weather Forecast.* **2011**, *26*, 868–884. [CrossRef]
54. Ying, M.; Zhang, W.; Yu, H.; Lu, X.; Feng, J.; Fan, Y.; Zhu, Y.; Chen, D. An overview of the China Meteorological Administration tropical cyclone database. *J. Atmos. Ocean. Technol.* **2014**, *31*, 287–301. [CrossRef]
55. Junker, N.W.; Hoke, J.E.; Sullivan, B.E.; Brill, K.F.; Hughes, F.J. Seasonal and geographic variations in quantitative precipitation prediction by NMC's nested-grid model and medium-range forecast model. *Weather Forecast.* **1992**, *7*, 410–429. [CrossRef]